Characterisation, analysis and technical solutions of a biomass-gas fed PEM fuel cell system

Geers, M.P.A.

Award date:
2006

TU/e technische universiteit eindhoven

Capaciteitsgroep Elektrische Energietechniek
Electromechanics & Power Electronics

Master of Science Thesis

Characterisation, Analysis and technical solutions of a biomass-gas fed PEM fuel cell system

M.P.A. Geers
EPE.2006.A.07

Coaches:

Ir. P.J.H. Wingelaar
Dr. J.L. Duarte
Ir. M.A.M. Hendrix

October 2006

/ faculteit elektrotechniek

Abstract

Polymer Electrolyte Membrane (PEM) fuel cells can be used as an alternative power source. These fuel cells often use platinum as catalyst and require hydrogen to produce energy. Hydrogen can be produced in various ways, such as gasification of biomass and via electrolysis. A by-product of gasification is carbon monoxide (CO). CO adsorbs easily to platinum, causing an obstruction of the catalyst in the fuel cell, thus reducing its performance.

The goal of the research is to regenerate a CO poisoned PEM fuel cell by means of electrolysis. This is done by applying a negative voltage pulse on a poisoned cell. A converter is designed and built to generate these pulses and performed within design specifications.

It is measured that two out of four cells of one PEM cartridge can be regenerated by applying negative voltage pulses to the cells. However, it is uncertain whether the process responsible for the regeneration is electrolysis. The other cells remained unaffected. It is also determined that periods of no load help in the regeneration of poisoned cells.

Table of contents

1 Introduction

This report describes the subject and results of my master thesis: *Characterisation, Analysis and technical solutions of a biomass-gas fed PEM fuel cell system.* The work has been done in the group Electro mechanics and Power Electronics (EPE) in the department of Electrical Engineering of the Eindhoven University of Technology (TU/e).

Within the group, research is conducted on modelling steady-state and dynamic behaviour of a Polymer Electrolyte Membrane (PEM) fuel cell. Recently, small- and large signal behaviour was combined with steady-state characteristics in one model. The parameters of this model can be found using Electrochemical Impedance Spectroscopy (EIS), step-responses and steady-state characteristics **[1]**.

The research project includes the use of synthetic gas, simulating the output of a biomass gasification system. The main gas component of this gas mixture is hydrogen (H_2), the fuel for a PEM fuel cell. However, it also contains trace amounts of carbon monoxide (CO). One of the disadvantages of using PEM fuel cells is that the platinum catalyst is extremely sensitive to CO poisoning, causing a reversible deterioration of the overall performance **[7]**.

The goal of this master project is to regenerate a PEM fuel cell from CO poisoning by means of periodically electrolysing the water contained inside the membrane, with a power electronic converter. The existing electrical model of the system should be adjusted based on the results gathered.

1.1 Project background

With the rise of oil prices and the call for sustainable energy sources, hydrogen is considered as a promising alternative fuel. Electricity can be generated from hydrogen and oxygen in a fuel cell with water as by-product, hence this technology has the potential to be very environmentally friendly **[25]**. The fuel cell is starting to rival the internal combustion engine (ICE) more and more in terms of power density. This makes it a viable alternative power source in decentralised power generation units and in transportation applications.

However, there is no infrastructure available for large scale hydrogen generation, distribution and storage at the present. Therefore, it is unlikely that pure hydrogen will be used as a large scale fuel on the short term. However, hydrogen can be produced with on-board hydro-carbon reformers. The major products will be carbon dioxide (CO_2) and hydrogen (H_2) **[2]**.

1.2 Electrochemistry basics

The fuel cell is an electrochemical device. In order to understand some of the theory presented in this report, brief descriptions of several electrochemical concepts are presented here.

1.2.1 Anode and Cathode

In electrochemistry there is a convention where the electrode at which electrons are released (where oxidation takes place) is called the anode. The electrode where electrons are used (where reduction takes place) is called the cathode **[3]**. This translates into electrical engineering terms as: the anode being the electrode where the electrical current is flowing into and the cathode the electrode where the current is originating from.

1.2.2 Open circuit voltage / electromotive force (emf)

In an electrochemical cell, an electrical potential is created between two dissimilar metals. This potential is a measure of the energy per unit charge which is available from the oxidation/reduction reactions to drive the reaction. The cell potential (emf) has a contribution from the anode, which is a measure of its ability to lose electrons, its "oxidation potential". The cathode has a contribution based on its ability to gain electrons, its "reduction potential". The cell potential is defined as the sum of the oxidation and reduction potentials (1.1) **[4]**.

$$E^{\circ}_{cell} = E^{\circ}_{ox} + E^{\circ}_{red}. \tag{1.1}$$

However, the individual electrodes cannot be determined in isolation. Therefore, the potential of the reaction at an electrode is measured with respect to a standard hydrogen electrode (SHE) **[4]**. This is considered to be the electrochemical equivalent of "ground" or "mass" in electrical engineering terms. The reaction that takes place at the SHE is (1.2)

$$2H^{+}(aq) + 2e^{-} \rightleftarrows H_2(g). \tag{1.2}$$

If the reaction is reversed, this potential is necessary to let the reaction occur.

1.3 The PEM Fuel cell

A fuel cell is a device that can produce electricity from chemical reactions. A polymer electrolyte membrane (PEM) fuel cell, also known as a proton-exchange membrane fuel cell, consists primarily of five parts. Figure 1-1 shows these parts schematically. Metal plate *a* (anode) is the negative terminal of the fuel cell, metal plate *e* (cathode) is the positive terminal of the fuel cell. Plates *b* and *d* are diffusion layers, consisting of carbon with a thin layer of platinum catalyst. Finally, plate c is the polymer membrane in a rubber gasket **[5]**.

Two chemical equations describing the anode (1.3) and cathode (1.4) reaction result in the overall reaction of the PEM fuel cell,

$$2H_2 \rightarrow 4H^+ + 4e^-, \qquad E^\circ_{ox} = 0V, \tag{1.3}$$

$$O_2 + 4e^- + 4H^+ \rightarrow 2H_2O, \qquad E^\circ_{red} = 1.23V, \tag{1.4}$$

$$2H_2 + O_2 \rightarrow 2H_2O, \qquad E^\circ_{cell} = 1.23V. \tag{1.5}$$

Figure 1-2 shows these reactions in a schematic representation of a fuel cell. Four protons (H^+) and four electrons (e^-) are created from two hydrogen molecules, under the influence of the platinum catalyst **[6]**.

The membrane has the property that only the hydrated protons (or hydronium ions) are let through. The electrons will thus move through the anode and via an electrical circuit to the cathode side. The protons will attach to water molecules, forming hydronium ions (H_3O^+) which transport the protons through the membrane to the cathode side, thus freeing a catalyst site for continuation of the reaction. On the cathode side, oxygen (O_2) is split into two O^{2-} ions which attach to the platinum catalyst. After that, the electrons and protons combine with the oxygen ions to form two water molecules **[6]**.

A practical fuel cell device consists out of stacks of individual fuel cells. The individual cells are placed in series to obtain a higher output voltage. Several of these stacks can again be placed in series to get an even higher voltage. During this project, cartridges are used which contain a stack of four cells.

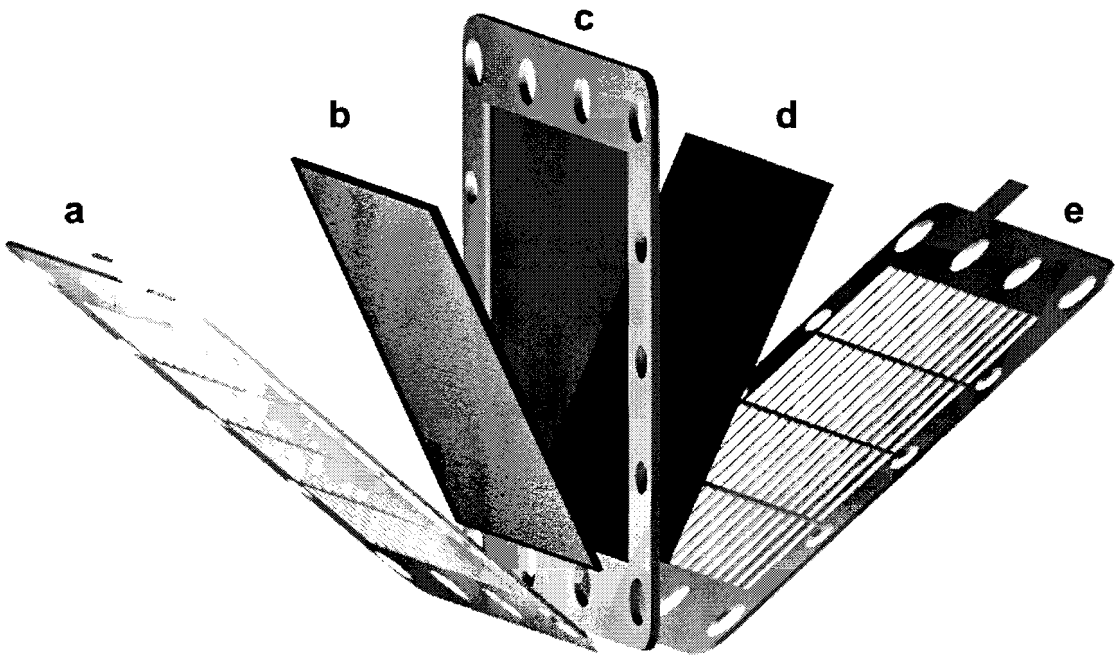

Figure 1-1: Schematic representation of a PEM fuel cell.

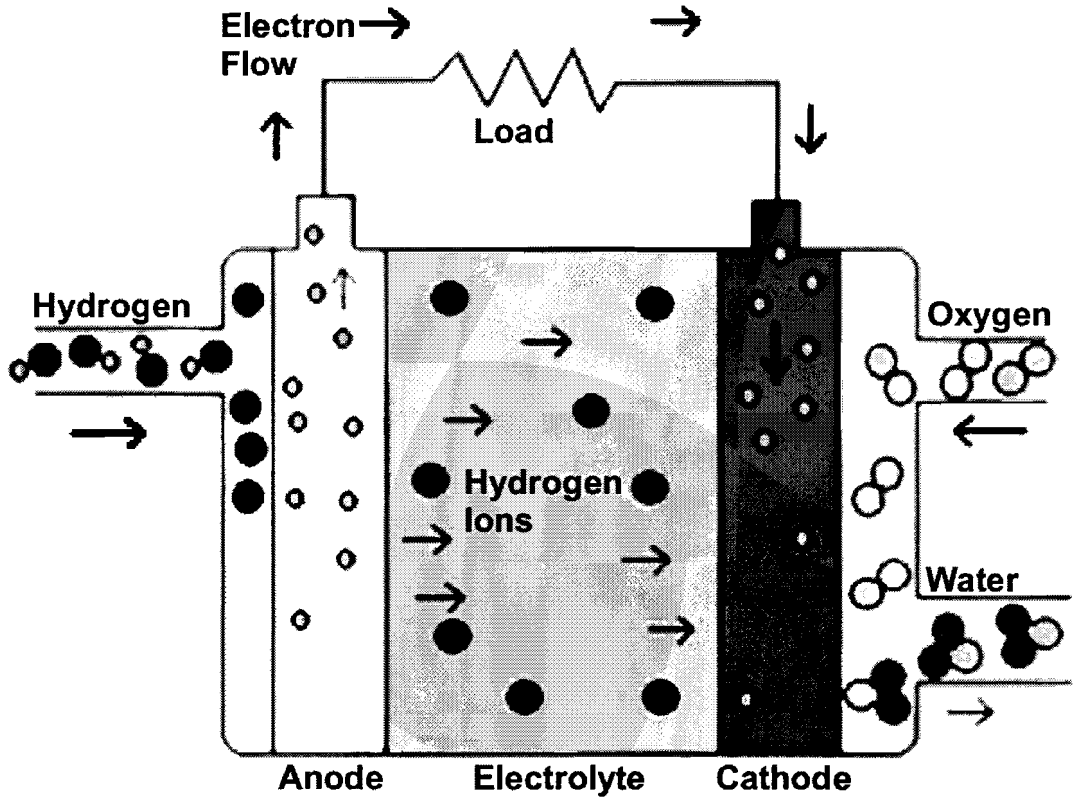

Figure 1-2: A schematic overview of a PEM fuel cell

1.4 CO poisoning

The major products of a hydro carbon reformer are CO_2 and H_2. However, it also contains carbon monoxide (CO) (a few percent). The CO adsorbs well to the platinum catalyst. Due to which, the fuel cell will be more and more hindered in its operation until no power can be drawn from it, hence the term "poisoning" **[7].** This hindrance is caused by occupation of free catalysis sites by the CO. The adsorbed CO also lowers the hydrogen reactivity via dipole interactions and electron capture **[7]**.

Several methods have been devised to free the catalysis sites of adsorbed CO. These include the oxidation of the CO and raising the temperature. Raising the temperature is not very practical. A higher cell temperature leads to greater water loss to the exhaust gas streams as more water evaporates, causing drying of the porous media inside the cell **[8]**. This in turn increases the ionic resistance, which gives rise to the voltage drop due to ohmic losses **[9]**.

There are, however, several other known methods to oxidise adsorbed CO. The first is by adding pure oxygen to the fuel stream **[10], [11], [12]**. This introduces a gas mixture in which chemical oxidation of hydrogen and CO can take place. Only a small amount of the oxygen in the fuel stream reacts with the adsorbed CO, causing the fuel cell to heat up as other parts of the added oxygen react with the hydrogen, thus reducing efficiency even more.

The second method is by raising the anode potential. If the anode potential is high enough an electrochemical oxidation of CO takes place. It is however unpractical to operate a PEMFC at such high anode potentials, as it has a very low efficiency at that operating level **[7], [12]**. It is, however, possible to lower the potential required to induce this reaction. This can be accomplished by adding ruthenium (Ru) to the platinum catalyst. This lower activation potential can have the additional effect of self-oxidation **[13]**. This is a phenomenon where the anode potential rises due to the CO poisoning, causing the oxidation of CO. An oscillatory behaviour will become visible as the potential will return to normal values after oxidation and rises again till the next oxidation takes place. This phenomenon has been the basis for another method to oxidise the adsorbed CO. By briefly applying a pulse in the load of the PEMFC, the anode potential will be briefly raised high enough to oxidise the CO. The performance of a PEMFC fed with H_2/CO fuel can be greatly increased by periodically pulsing the load. The consequences of this might be that the total system complexity can be reduced, as the reformat gas does not have to be as pure as before **[14], [15], [16], [17]**.

1.5 Electrolysis

Electrolysis is an electrochemical redox reaction. This implies that it consists out of two linked reactions. Electrons will be released at one electrode and used at the other. These two redox half reactions are (1.6) and (1.7)

$$2H_2O \rightarrow O_2 + 4H^+ + 4e^-, \qquad E^\circ_{ox} = -1.23V, \tag{1.6}$$

$$4H_2O + 4e^- \rightarrow 4OH^- + 2H_2, \qquad E^\circ_{red} = -0.83V, \tag{1.7}$$

$$2H_2O \rightarrow O_2 + 2H_2, \qquad E^\circ_{tot} = -2.06V. \tag{1.8}$$

Here (1.6) and (1.7) are respectively the anode and cathode reactions **[18]**. It is clear that oxygen is produced at the electrode where the electrical current is entering the system. The overall reaction (after an acid-base reaction has taken place) is then (1.8).

With the fuel cell in normal operation (generator mode) the reactions (1.3) and (1.4) take place at respectively the anode and cathode. The hydrogen fuel is used at the anode (1.3), which implies that the CO contamination will also take place at the anode. In order to generate oxygen at this anode by means of electrolysis, the electrical current should keep the same direction, whereas the cell voltage should be reversed. This can be accomplished by putting a voltage or current source in parallel with the affected cell. There should thus be the ability to switch this source in parallel with a specific cell and this source should be able to pulse the current or voltage.

The electrolysis reaction described above is based on a base-reaction. The fuel cell membrane, however, is assumed to work via acid reactions. It is therefore expected that the electrolysis will take place via the inverted fuel cell reactions. Thus reactions (1.3) and (1.4) but from the right to the left.

2 Power electronic converter

*The theory presented in this chapter related to the design of the fly-back converter is primarily based on the theory presented in **[19]** and **[20]**.*

A power electronic converter can be used to periodically apply pulses to the PEM fuel cell, in order to induce brief periods of electrolysis. This converter can be placed in parallel with one of the cells of a fuel cell stack. It is therefore necessary that the output of this converter is *not* grounded. An isolated fly-back topology complies with these boundary conditions. The fly-back is a popular topology as it requires very few power electronic components.

A fly-back converter is a modified Buck-boost converter, where the inductor is replaced with a pair of coupled inductors, or fly-back transformer as is shown in Figure 2-1. Here, the fly-back transformer is depicted by an ideal transformer with a magnetising inductor L_m in parallel with the primary transformer coil.

The converter works by turning the primary switch $S1$ on, causing the voltage U_s to be applied over the inductor L_m. This causes a current to flow with a constant non-zero slope. During this time, the diode on the secondary side will be negatively biased and no current will flow through it. As a result, energy will be stored in the transformer. After a time, the switch will be turned off and the diode at the secondary side will become positively biased. The stored energy will then be released via the secondary side of the transformer to the output capacitor and the load.

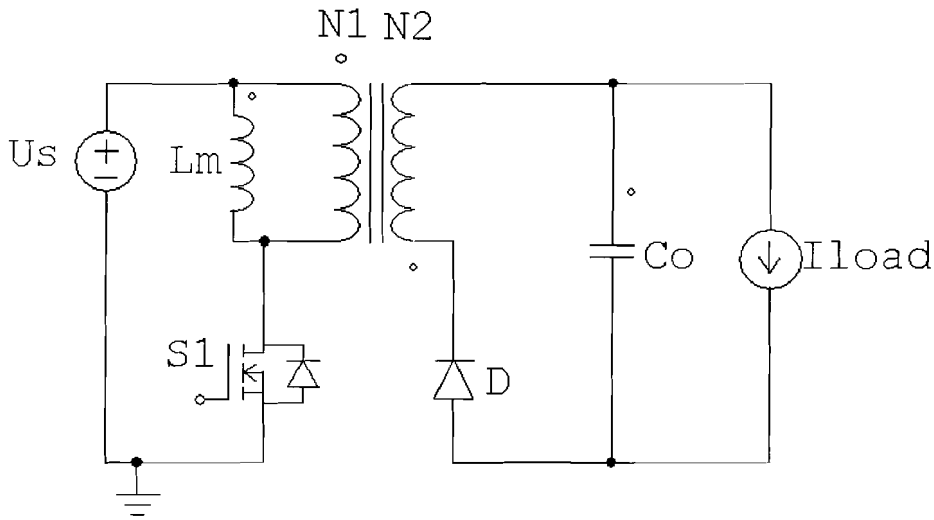

Figure 2-1: Ideal isolated fly-back converter

The component values of the converter can be derived from a set of desired voltages and currents. The analysis of the circuit is split up into two parts. The first is when the primary switch is on and the second when it is off. Continues Conduction Mode (CCM) is assumed. This means the current through the magnetizing inductor will never reach zero. Furthermore, the input and output voltages will be assumed constant and the circuit to be at steady-state.

2.1 System description

The period where the primary switch is turned on, will be referred to as "Mode I" and the period where it is turned off as "Mode II". The duty-cycle D describes the lengths of Mode I and II as a function of the switching period, with t_{on} the on-time and T_s the switching period.

$$D = \frac{t_{on}}{T_s}. \tag{2.1}$$

The voltage and current waveforms described below are shown in Figure 2-2 and Figure 2-3 together with the time spans DT_s and $(1-D)T_s$, which indicate the different modes. The current through the primary switch is indicated by $I_{s,prim}$ and the one through the secondary switch (D) or diode by $I_{s,sec}$.

During Mode I, the voltage over the magnetizing inductor L_m will be equal to the source voltage U_s. The resulting current as a function of time **(2.6)** can be derived from the inductor relationship **(2.4)**. $I_m(0)$ is the current level at the start of the switching period. The maximum current reached at the end of Mode I $\left(t = DT_s, I_{m_{max}}\right)$ will be equal to **(2.8)**.

During Mode II, the diode will conduct and the voltage over L_m will be **(2.3)**, as the voltage on the secondary side is transformed with a factor n to the primary side. This results in a decrease of the current according to **(2.5)** and **(2.7)**. Both **(2.6)** and **(2.7)** are referred to the primary side.

The energy stored during Mode I should be equal to the energy released during Mode II. This results in equation **(2.9)**. By solving this equation, a relationship can be found between U_o, U_s, D and n **(2.10)** **[19]**.

Mode I		Mode II	
$U_{L_m} = U_s$	(2.2)	$U_{L_m} = -nU_o$	(2.3)
$U_s = L_m \frac{di_m}{dt}$	(2.4)	$-nU_o = L_m \frac{di_m}{dt}$	(2.5)
$i_m(t) = I_m(0) + \frac{U_s}{L_m} t$	(2.6)	$i_m(t) = I_{m,\max} - \frac{nU_o}{L_m} t$	(2.7)
$I_{m,\max} = I_m(0) + \frac{U_s}{L_m} DT_s$	(2.8)	$\frac{nU_o(1-D)T_s}{L_m} = \frac{U_s DT_s}{L_m}$	(2.9)

$$\frac{U_o}{U_s} = \frac{D}{(1-D)n} \quad (2.10)$$

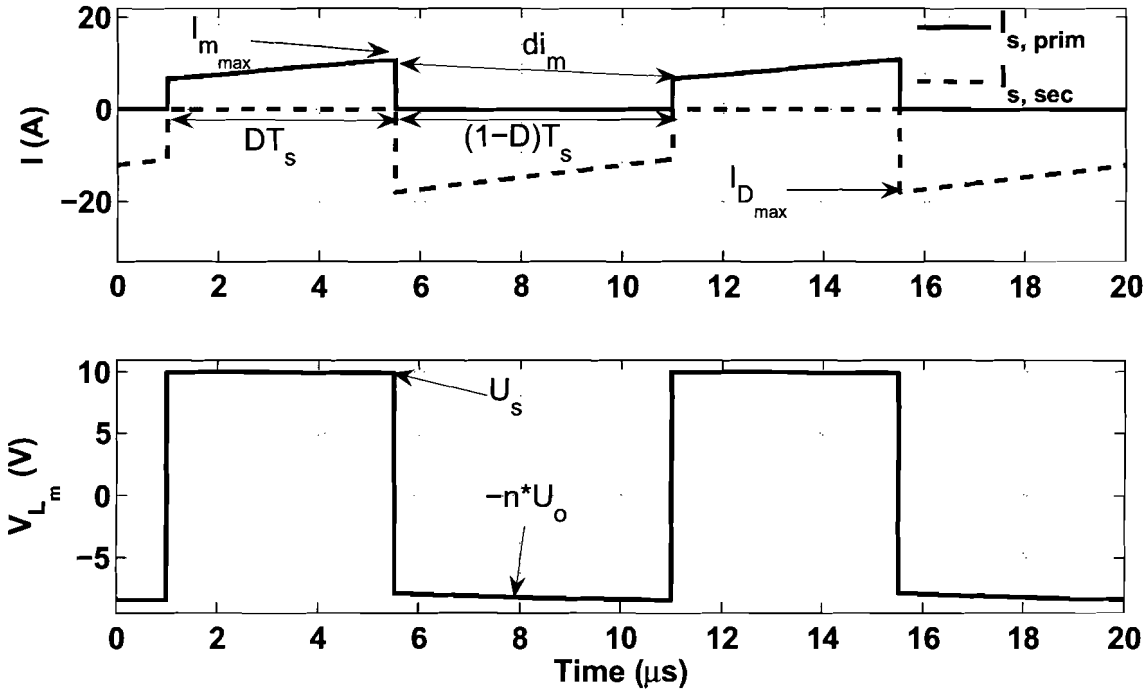

Figure 2-2: Current and voltage waveforms of an ideal isolated fly-back converter

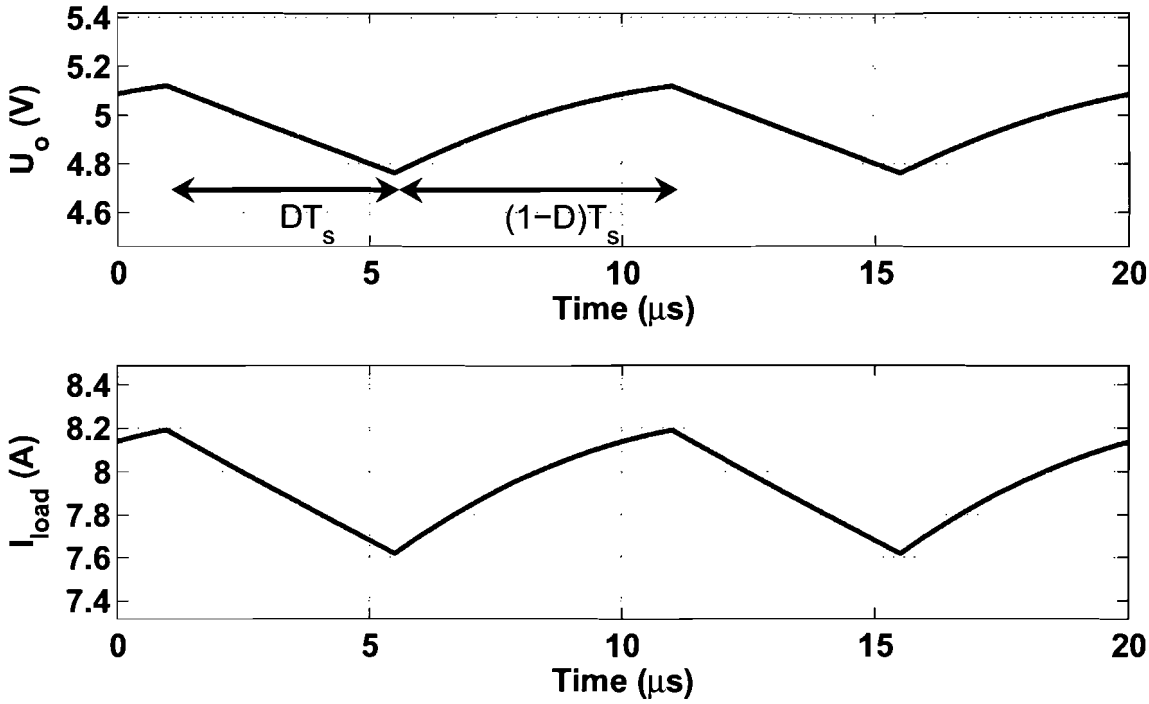

Figure 2-3: Output waveforms of an ideal isolated fly-back converter

2.2 Component calculation

Several boundary conditions are needed before the components of the converter can be calculated. These boundary conditions include values for U_o, U_s, D and I_o. The circuit components can be calculated from these parameters.

2.2.1 The transformer ratio n

With a given U_s, U_o and D the transformer ratio n can be determined from equation (2.10):

$$n = \frac{D}{(1-D)} \frac{U_s}{U_o}. \tag{2.11}$$

2.2.2 The magnetising inductor L_m

In steady-state operation the charge transported through the diode during Mode II should be equal to the charge used by the load during a full switching period

$$I_{load} T_s = \bar{i}_D (1-D) T_s. \tag{2.12}$$

According to the transformer relationship $i_1 N_1 = i_2 N_2$ the average diode current will be n times the average magnetising current. Therefore, the required average magnetising current $\bar{i}_m$ will be **[21]**

$$\bar{i}_m = \frac{1}{n(1-D)} I_{load}. \tag{2.13}$$

It is shown in equation (2.6) that the slope of the magnetising current is determined by the size of the magnetising inductance. Therefore, the ripple current $2\Delta i_m$ should be chosen so that it satisfies the specific design. The maximum currents will then be

$$\begin{aligned} I_{m,\max} &= \bar{i}_m + \Delta i_m, \\ I_{D,\max} &= n \cdot I_{m,\max}. \end{aligned} \tag{2.14}$$

In order to accomplish the $2\Delta i_m$ ripple, (2.4) can be used to determine the size of the magnetising inductance **[21]**

$$2\Delta i_m = \frac{U_s}{L_m} DT_s \rightarrow L_m = \frac{U_s DT_s}{2\Delta i_m}. \tag{2.15}$$

2.2.3 The output capacitor C_o

The output capacitor size is dependent on the allowed voltage ripple ΔU_o. This voltage ripple is dependent on the load current I_{load} and the duty-cycle D:

$$i = C\frac{\Delta V}{\Delta t} \rightarrow \Delta U_o = \Delta t \frac{I_{load}}{C_o} = \frac{DT_s I_{load}}{C_o}. \tag{2.16}$$

2.2.4 Leakage inductance

The coupling between the primary and secondary coil of the fly-back transformer may not be ideal, resulting in a leakage flux which does not contribute to the energy transfer from the primary to the secondary side. It does however store a small amount of energy. As is shown in Figure 2-4, the energy stored in this leakage inductance L_l does not have a path to ground or the source when the switch is turned off. The result is that the parasitic capacitance of the switch is charged rapidly to a high voltage, causing the switch to breakdown.

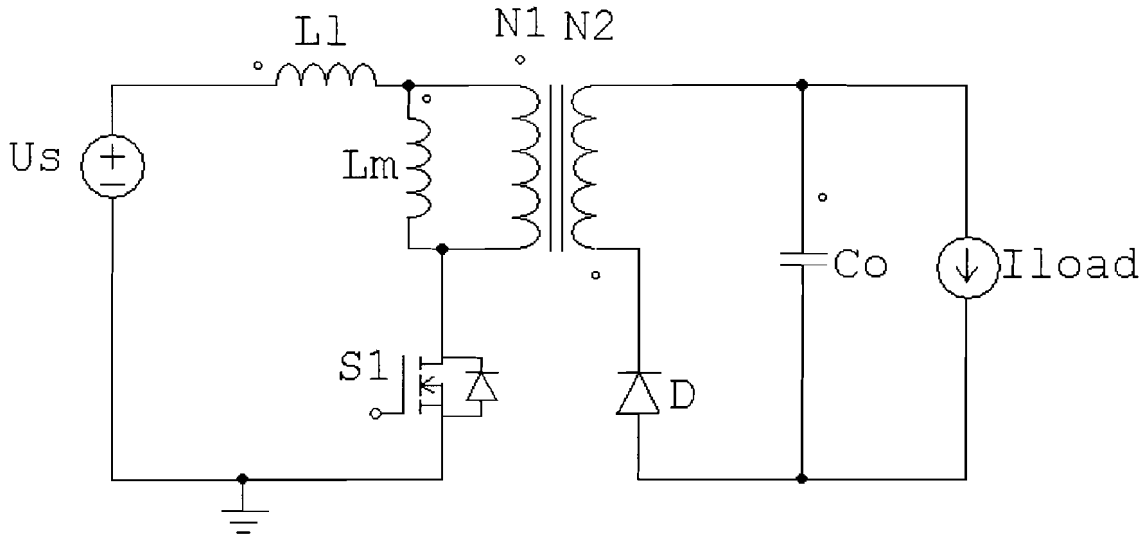

Figure 2-4: Fly-back converter with leakage inductance

2.2.5 Snubber

To prevent this breakdown, a conduction path should be available at turn-off. A method to provide this path is to include a snubber in the circuit. The energy in the leakage inductance can be redirected by or dissipated in this snubber. This allows the excess energy to be dissipated at a predefined area in the converter.

The snubber used in this converter does not have to be regenerative, as it is not a goal to reach a very high efficiency. Therefore a passive dissipative snubber is chosen. There are basically three types of passive snubbers, shown in Figure 2-5: the rate of rise control, the voltage clamp and the damping snubbers **[22]**.

The damping snubber, Figure 2-5a, will put a constant drain on the system with every voltage change and therefore hinder circuit operation and efficiency. The voltage clamp snubber, Figure 2-5b, will limit the voltage spike caused by the release of the energy stored in the leakage inductance. During the release of this energy, the voltage will be effectively clamped to the constant voltage over the snubber capacitor. Finally, the rate-of-rise control snubber, Figure 2-5c, can be used to both clamp the drain voltage to a specific value and limit the rate at which this voltage rises **[22]**.

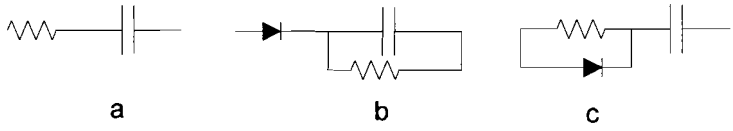

Figure 2-5: a) damping snubber b) voltage clamp snubber c) rate of rise control snubber

In first instance, the voltage clamp topology was chosen. The disadvantage of the voltage clamp snubber is that oscillations will occur when the voltage drops below the clamp voltage. These oscillations are unwanted, as these might cause EMI problems. The snubber voltage and the voltage over the primary switch, as indicated in Figure 2-6, are shown in Figure 2-7. The first graph shows the voltages of a voltage clamp snubber with a long RC-time and the second one with a short RC-time. A long RC-time will allow for large oscillations. A short RC-time can be chosen to damp out the oscillations, but will also cause a continuous capacitive load of the circuit node at the drain of the MOSFET. This can be seen in the first graph where the switch voltage and the snubber voltage are the same during the time the switch is off.

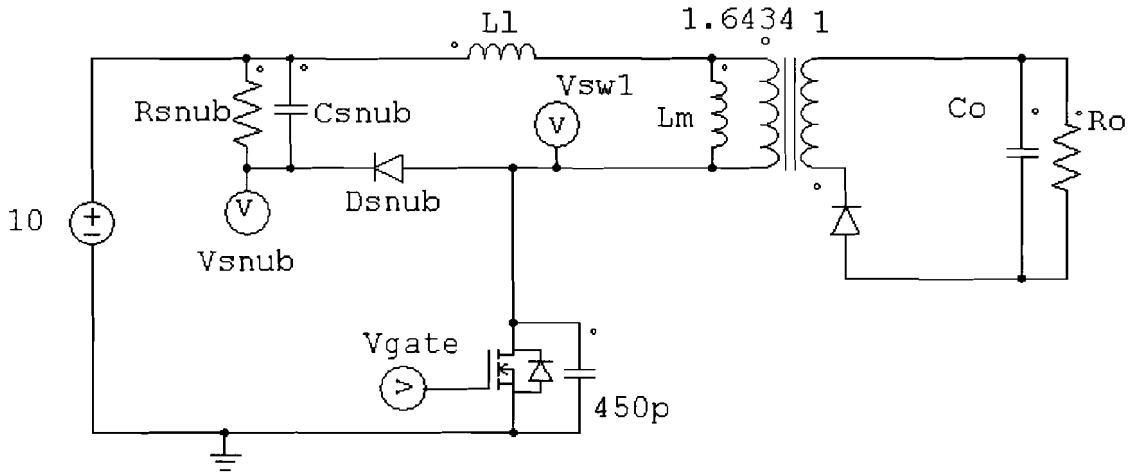

Figure 2-6: Isolated fly-back converter with a voltage clamp snubber.

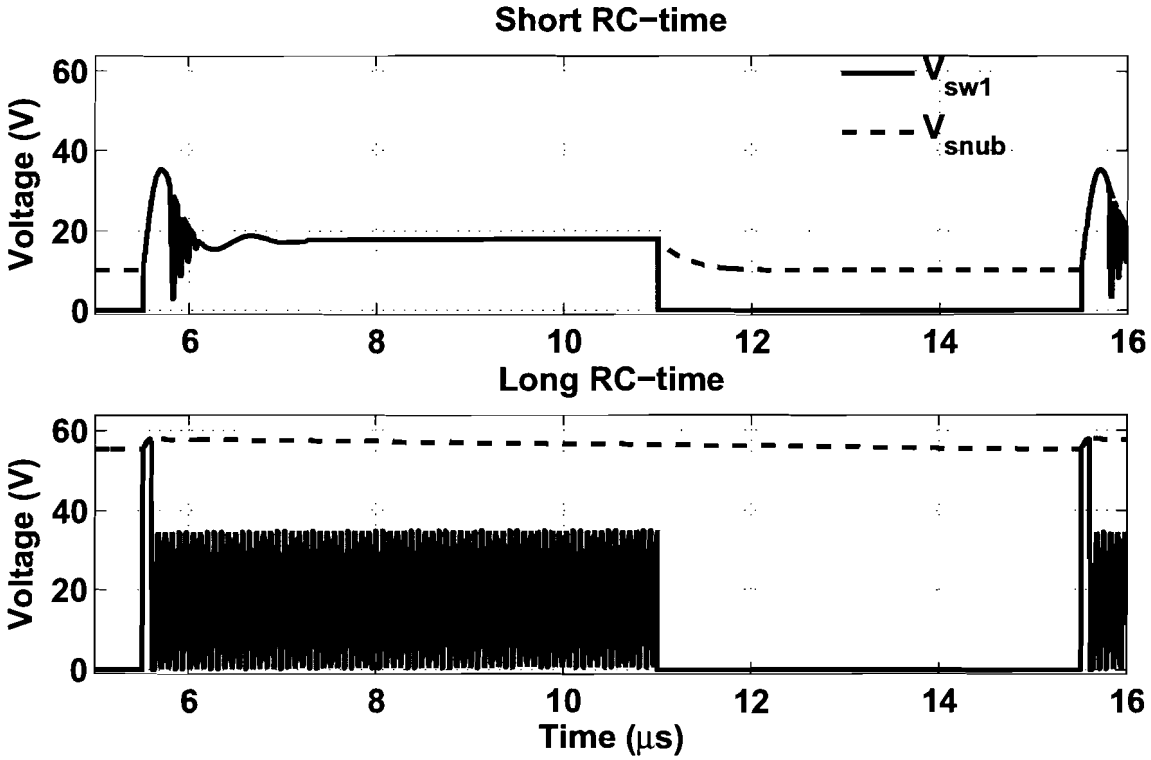

Figure 2-7: Typical waveforms when a voltage clamp snubber is used in a fly-back converter without damping.

The snubber has another function, which is preventing parasitic switching or increased switching times of the MOSFET. The rapid voltage rise at the drain might have a large enough dV/dt which causes a rise of the gate voltage via the parasitic gate-drain capacitance C_{gd}. Therefore, the rate at which the drain voltage rises, should be limited by the snubber. The snubber capacitor size will thus be a compromise between a high acceptable clamp voltage and a slow rate of rise to ensure proper turn-off of the MOSFET. The rate of rise control snubber will therefore be used in the circuit, as is shown in Figure 2-8.

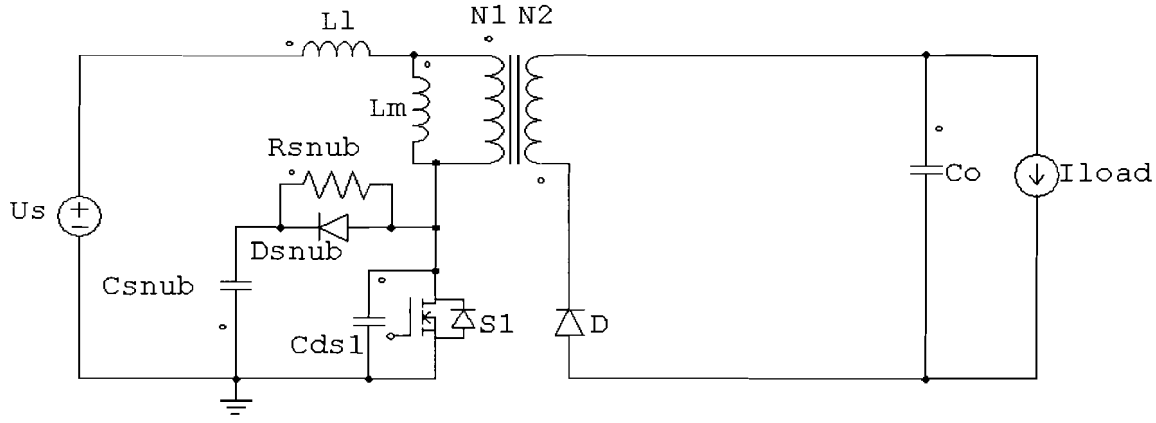

Figure 2-8: Fly-back converter with rate of rise control snubber and parasitic elements

With this configuration, the voltage spike over the MOSFET will become a relatively low frequency oscillation. The snubber resistor R_{snub} should be chosen such that this oscillation is damped quickly, preventing high frequency oscillations, such that high frequency noise is eliminated. Furthermore, the RC-time should be short enough to ensure the ability to use small duty-cycles. Short RC-times and oscillation reduction coincide with relatively high clamp voltages and quick voltage rises and thus the possibility of a unfavourable MOSFET turn-off. Longer RC-times and good oscillation reduction coincide with slow rate of rise and a lower clamp voltage and thus an increase of the minimum duty cycle. An example of the effects of a rate of rise snubber on the drain voltage of the primary switch is shown in Figure 2-9.

2.2.6 Bi-directional power transfer

As is discussed in the introduction, pulsing the load of the fuel cell could be beneficial to the performance of the fuel cell. It is also indicated that this does not work with the catalyst available in the PEM under test. It is, however, not known if this technique will be beneficial in combination with the electrolysing technique. Therefore the option of feeding back energy to the input of the converter is implemented. This is done by replacing the secondary diode by a second MOSFET. The MOSFET in this set-up has a parasitic capacitance similar to the one at the primary side. This will introduce an oscillation between the leakage inductance divided by N^2 and the parasitic capacitance as soon as the combination of the MOSFET and its anti-parallel diode stops conducting. A second snubber is added to damp this oscillation. The resulting converter topology is shown in Figure 2-10.

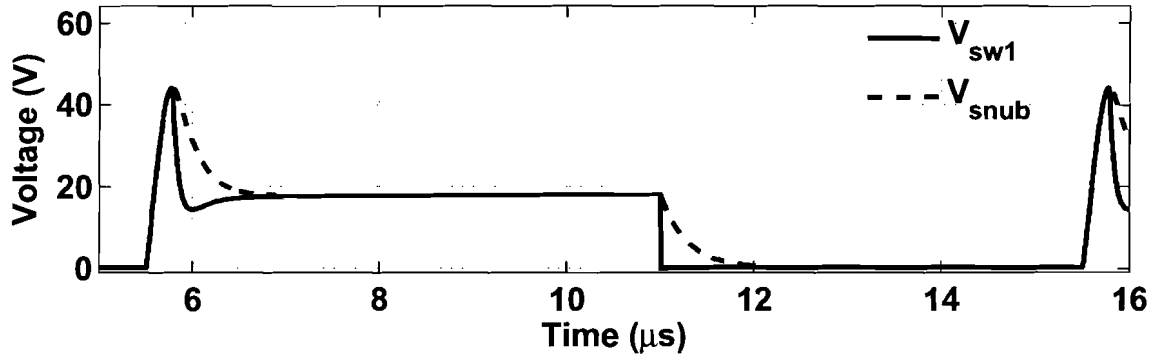

Figure 2-9: Typical waveforms when a rate-of-rise-control snubber is used with a fly-back converter.

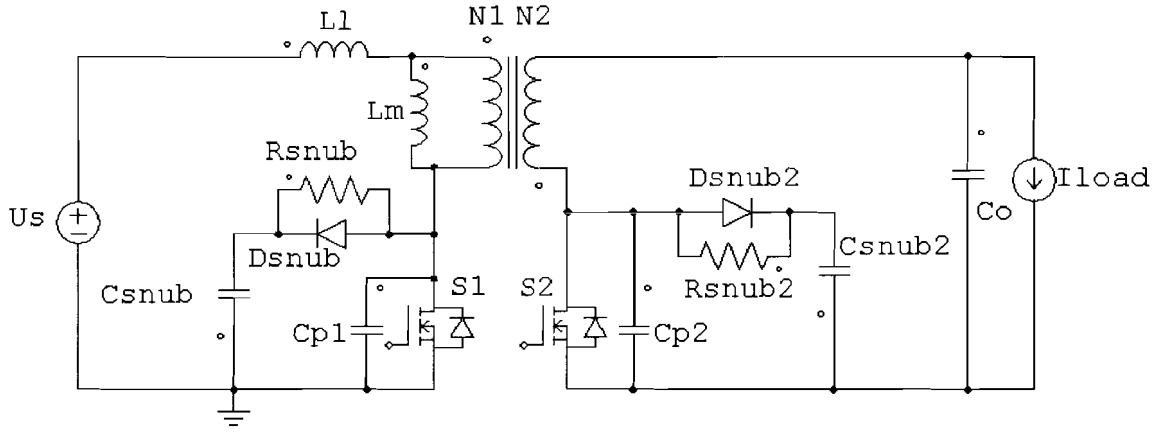

Figure 2-10: Fly-back converter with a dual (active) switch topology

2.3 Design considerations for the transformer

In the previous section, equations have been derived for the winding ratio and the magnetisation inductance of the transformer. However, a transformer exists only of two coils and a core. Additionally, an air gap in the core is needed to store the energy being transferred by the converter during each switching period. The physical aspects of the core put a limit on the maximum allowable flux density B_{max}. Furthermore, the size of the air gap determines the maximum amount of energy that can be stored in the transformer. By combining these limitations with the desired L_m and n a result for the number of windings is found.

The required L_m, n and maximum current I_{max} through the transformer, are determined to comply with the desired functionality of the converter. Afterwards an appropriate core is selected. In this case, however, an available bobbin and core are selected and the design is adjusted accordingly. The equations needed for dimensioning the transformer are derived in Appendix A. Given the design parameters from Table 1, the numbers of turns needed in combination with the RM-12 core are:

$$N_{1,max} \approx \frac{i_{max} L_m}{B_{max} A_e} = \frac{9.31 \cdot 21.44 \cdot 10^{-6}}{270 \cdot 10^{-3} \cdot 146 \cdot 10^{-6}} = 5.06 \approx 5, \tag{2.17}$$

$$N_2 = \frac{N_{1,max}}{n} = \frac{5.06}{1.922} = 2.63 \approx 3. \tag{2.18}$$

2.4 Converter component design and specification

Before the components of the converter can be dimensioned, values for the input (U_s V_{in}) and output (U_o) voltages, duty cycle (D), switching frequency (f_s) and output current (I_o) should be chosen.

However, a problem arises with the specification of the output parameters. No literature indicates the voltage-current characteristics of a PEM fuel cell used as an electrolyser, nor is it known how much power is needed. A voltage-current characteristic of a PEM electrolyser has been found **[23]**, which indicates a diode like curve. Furthermore, the converter should be dimensioned to force voltage onto the fuel cell. This has led to the output specification of I_0=8A and V_{out}=5V. The chosen switching frequency is 100 kHz. This allows for the use of a small transformer core and bobbin, for which the RM-12 has been chosen. The input voltage and current should be within reach of the available equipment. A maximum input current of 10A has been specified according to the available voltage sources.

It has been noted earlier in this report that the converter should also have the possibility to feed back energy into the source, in order to fulfil the system requirement, D should not exceed 0.5. This will provide a better symmetry in both modes of operation. Both the input voltage and duty cycle can be used to keep the input current within the specified limit.

It is now possible to design the converter. First, the transformer ratio is calculated with (2.11). Second, the different aspects of the magnetising current can be calculated, based on desired values. It is important not to make the maximum and average currents during the on-time too large. The reason for this is shown in (2.14), (2.15). The maximum current through the secondary diode or switch will be n times the maximum magnetising current. Furthermore, the ripple on the magnetising current is inversely related to the magnetising inductance L_m, which is directly related to the number of windings placed on the bobbin. A copper wire with a diameter of 1.6 mm is used for the coils. A wire this thick ensures low (DC) losses. It does, however, limit the number of windings to approximately 11 in one layer. Last, (A.14) shows that the number of windings allowed to make a certain magnetising inductance is directly related to the maximum current.

All the considerations above have led to the specifications and component values shown in Table 1. The calculated values are the result of the design parameters. The number of windings has been rounded towards the nearest integer, as it is not practical to make a transformer with 5.06 and 2.63 windings. The consequence is a slight difference in the values of L_m and n. This can be corrected by choosing a lower duty cycle, thus keeping the currents the same. It also becomes clear from Table 1 that the realised magnetisation inductance is about twice as low. During the calculations regarding the air gap only the middle leg has been taken into account,

whereas all three legs should have been taken into account, hence the factor two difference. This can again be compensated with an altered duty cycle. The result can be saturation of the transformer core. The point of saturation can be checked by rewriting (A.13) to (2.19):

$$i_{\max} = \sqrt{\frac{l_{gap} B_{\max}^2 A_e}{\mu_0 L_m}} = 14.6A. \tag{2.19}$$

It is obvious that with the realised L_m and corrected A_e saturation will not occur till a value beyond the original design parameters.

Table 1: Fly-back converter parameters

Electrical design parameters			Transformer design parameters		
U_s	10	V	$B_{\max}$	270**	mT
U_o	5	V	A_e*#	146***	mm^2
D	0.49		MLT	61***	mm
I_{load}	8	A	K_u	0.9***	
Δi_m	$0.14 \cdot \bar{i}_m$	A	l_{gap}	0.27	mm
f_s	100	kHz			
ΔU_o	$0.08 \cdot U_o$	V			
$U_{sw,\max}$	55*	V			
$I_{sw,\max}$	56*	A			
Calculated values			Realisable values	Realised values	
C_o	98	μF	100	106	μF
L_m	21.44	μH	21.18	10.344	μH
L_l	1.29	μH	1.06	316	nH
n	1.922		1.667	1.64	
N_1	5.06		5		
N_2	2.63		3		
$I_{m,\max}$	9.31	A			
$\bar{i}_m$	8.16	A			
U_{sw1}	19.608	V			
R_{snub}****	5	Ω		12//12	Ω
C_{snub}****	68	nF			nF
D	0.49		0.41	0.45	

* These include a safety margin to prevent failure of the switch due to too high voltages and currents.

** B_{max} is given as 300mT; the lower value specified in the table is a safety margin.

*** Parameters specified in data book **[24]**.

**** Derived from simulations.

*# This is the cross section of the middle leg of the core.

2.5 Converter simulation

Powersim's PSIM is used to simulate the converter. The voltage and current waveforms of the ideal isolated fly-back converter shown in Figure 2-1, can be seen in Figure 2-2 and Figure 2-3.

A more realistic simulation of the built converter can be obtained by including the snubbers, additional parasitical resistors and the gate driver. These resistors are estimated based on the resistivity of copper and the dimensions of the print tracks. Contact resistances have been neglected. The resulting PSIM schematic is given in Appendix B. A model of the gate-driver of the primary MOSFET is presented in Figure 2-11. The only MOSFET parameter that can be specified in PSIM is its on-resistance $R_{ds,on}$. Furthermore, it can only be controlled by an "on" or "off" control signal. The comparator (*Comp1*) compares the "gate voltage" with a reference of 4V (the threshold voltage). The switch is turned on when the gate voltage passes the 4V. The results are shown in Figure 2-12. The disadvantage of this topology is an instant turn-on of the MOSFET when the gate voltage reaches the 4V. The effects on the switching behaviour are shown in Figure 2-13. A spike in the current through the switch is visible at turn-on. This is caused by the almost instantaneous discharge of the charge stored in the parasitic capacitance C_{ds}. In practise, the switch will not turn on so abruptly and the parasitic capacitance will be discharged more smoothly over the on-resistance $R_{ds,on}$. This topology does show the effect of the fast rising drain voltage of the MOSFET, as is indicated in Figure 2-12.

Finally, the duty cycle needs to be increased to about 0.49 to compensate for the losses in the circuit.

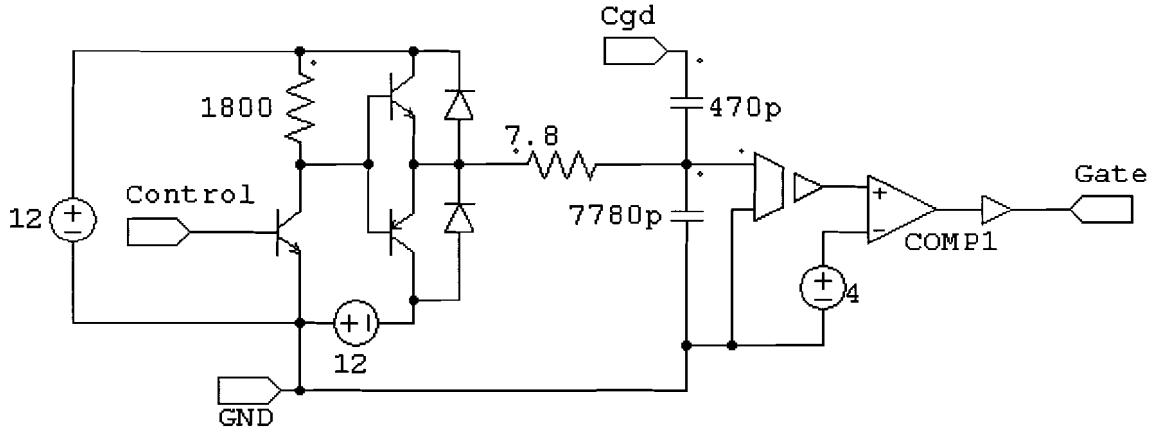

Figure 2-11: Gate driver simulation in PSIM

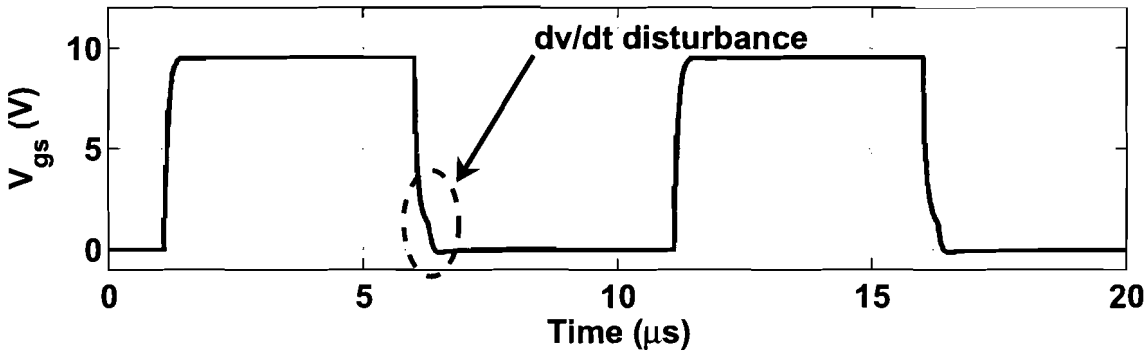

Figure 2-12: Gate driver output voltage as simulated in PSIM

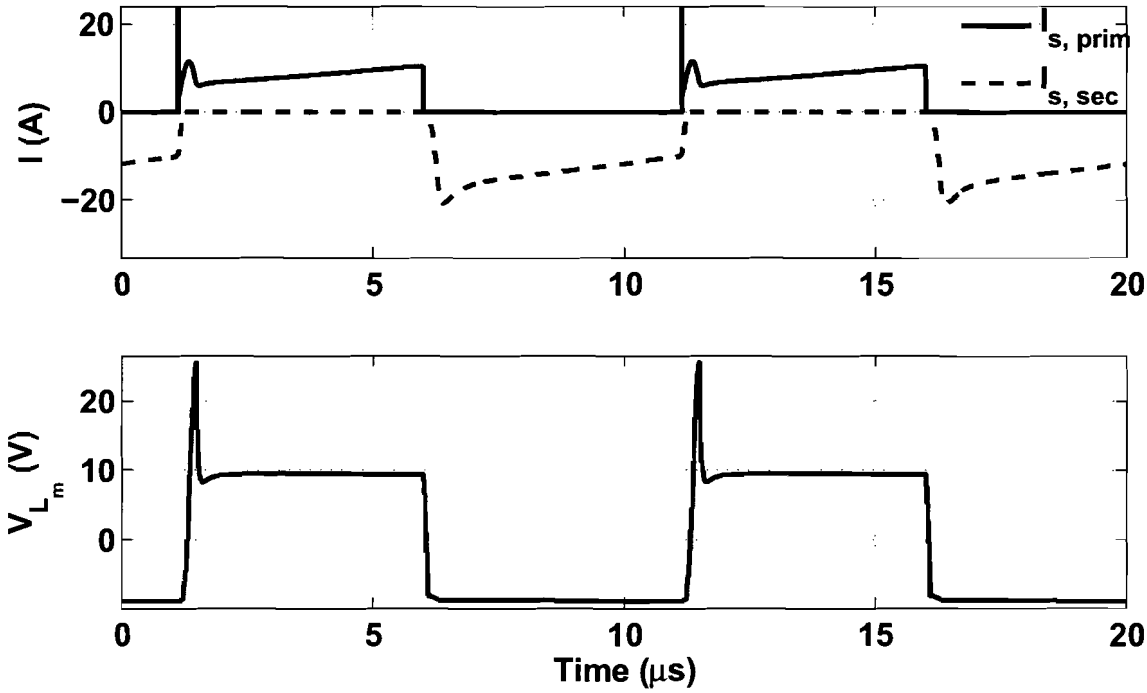

Figure 2-13: Realistic waveforms of an isolated fly-back converter with two snubbers

2.6 Control

The method chosen for the control of the converter is a PI controller implemented in Matlab Simulink. The controller output is limited by a saturation block to ensure the switches will always be switched. This prevents damage to the converter. An anti-windup circuit is implemented to prevent the integrator output growing to large values as soon as the saturation limit is reached. A total of three controllers are implemented. One for the output voltage, one for the output current and one for the cell voltage, which is shown in Figure 2-15. It is possible to switch between these controllers at any time. The downside of using multiple controllers is that the integrators might be at relatively high values at the time when controllers are switched. This is caused by a changing input and a constant reference while a controller is not in use. This is solved by making the inputs

of unused controllers zero and resetting their integrators. A flow diagram of the controller is shown in Figure 2-14.

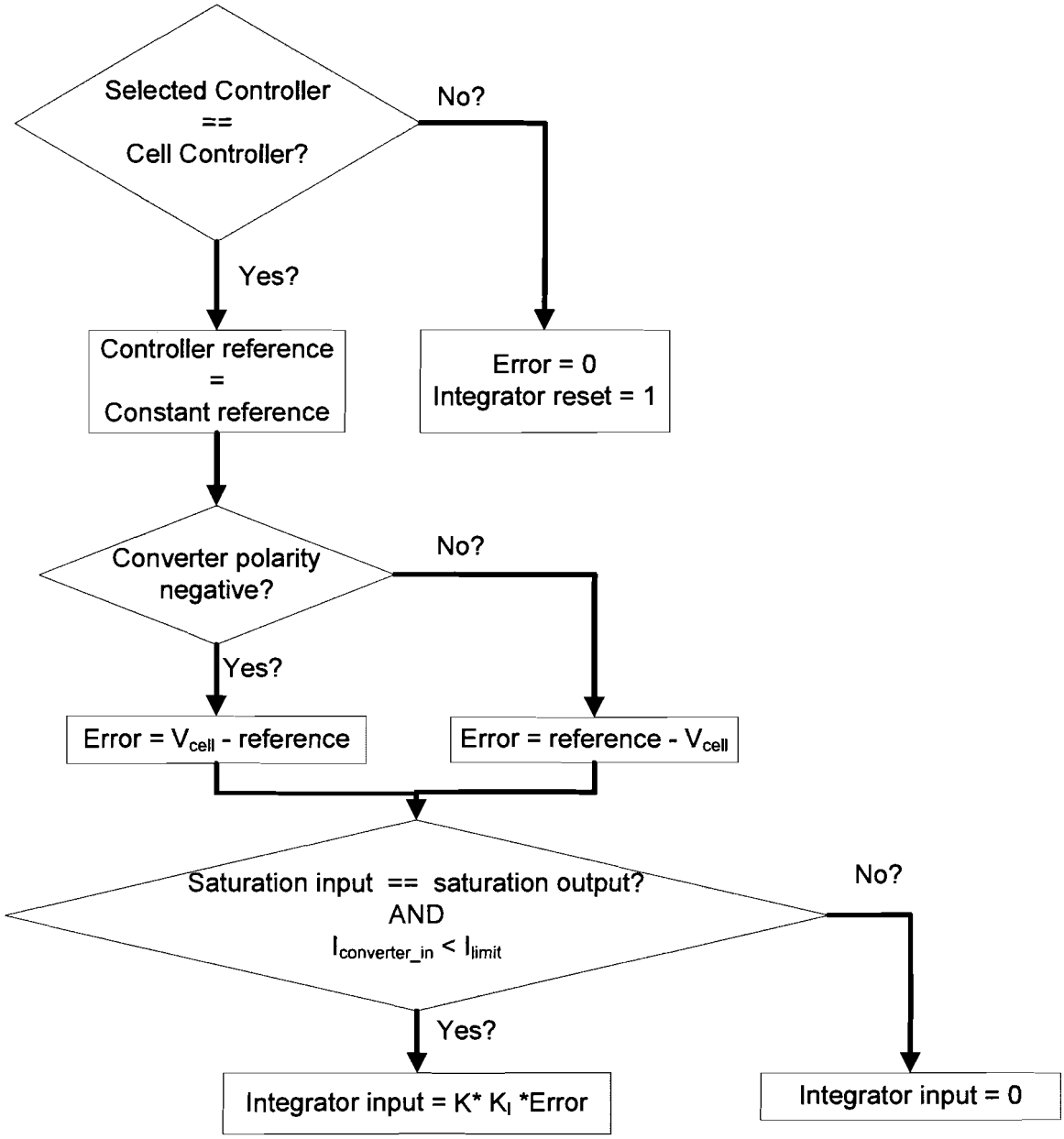

Figure 2-14: Flow diagram of the cell-voltage controller

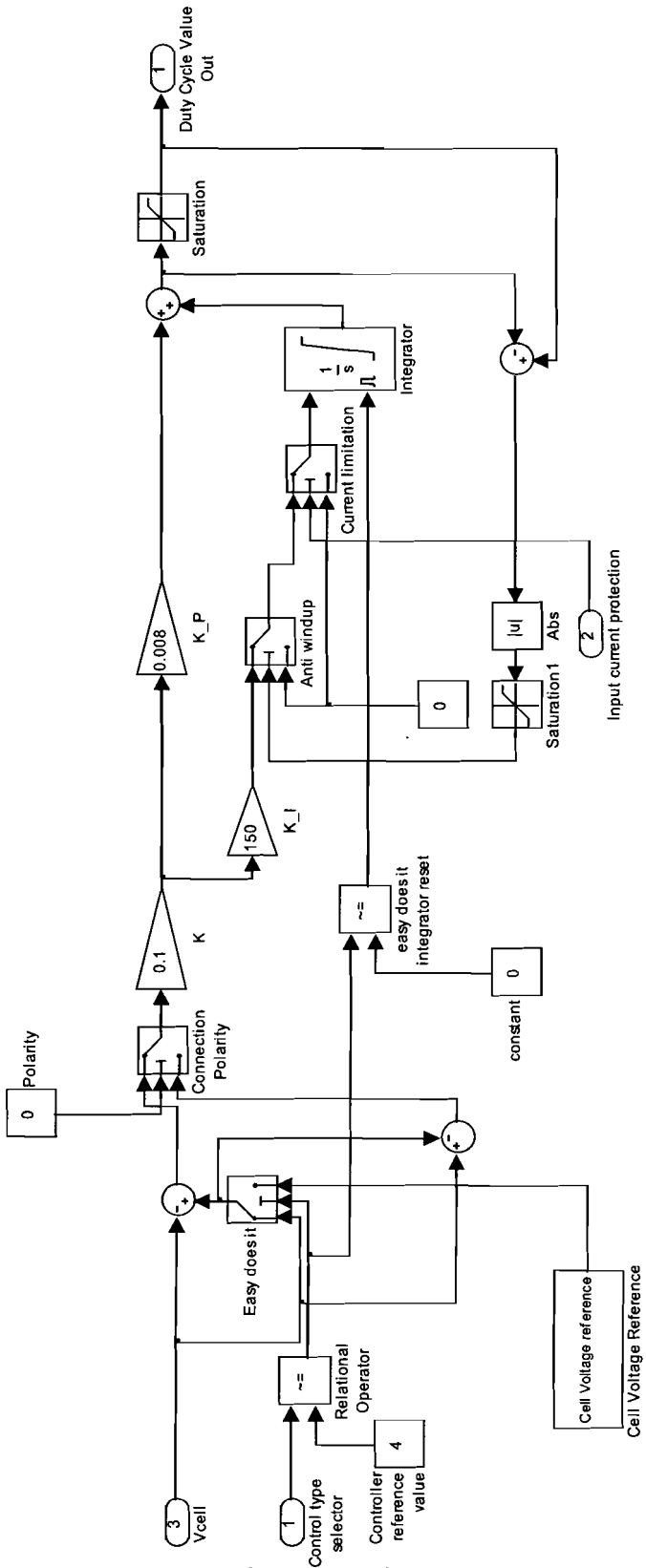

Figure 2-15: Cell-voltage controller

2.7 Additional circuitry

The (isolated) fly-back topology has been chosen for its simplicity and the low number of (power) components. However, in order to make the circuit work, additional circuitry is necessary. This includes the already mentioned gate drivers for the MOSFET's, voltage and current measurement sensors and the driving circuits for the relays, which allow the converter to switch between individual cells of the converter. These circuits are shown and described in Appendix C.

2.7.1 Relay switching set-up

As the H_2/CO fuel stream enters the fuel cell stack, it will pass through some cells in the stack sooner than others. Some evidence has been found that the CO concentrates itself primarily in one of the cells. This does not mean that the other cells will stay clean over time. It is necessary to have the ability to switch the converter dynamically in parallel with different cells. A relay circuit, Figure 2-16, has been designed to provide this ability. Two relays, indicated by the four sets, are switched simultaneously to switch the converter as a whole in parallel with a certain cell or to disconnect it from the fuel cell stack. This topology does not allow the converter to be switched in parallel to multiple cells though. If this functionality is needed, a re-wiring between the relay circuit and the fuel cell is needed. The drive circuitry for the relay coils can be found in Appendix C.

The thick black lines in Figure 2-16 indicate the current paths when the converter is regenerating the bottom cell of the fuel cell stack. Note that the voltage of the converter is opposite to that of the fuel cell. The voltage over the cell should become equal to the converter's output, minus the voltage drop over the connecting wires.

It should be noted that this topology does not allow the converter to act as a simple load by having a lower output voltage, but equal in sign, than the fuel cell. This design decision was made to put priority to the regeneration by electrolysis. Of course, if the switching between the individual cells is not needed, two sets of relays can be connected to the same cell with opposite polarities. This will provide both load and reversing polarity functionality.

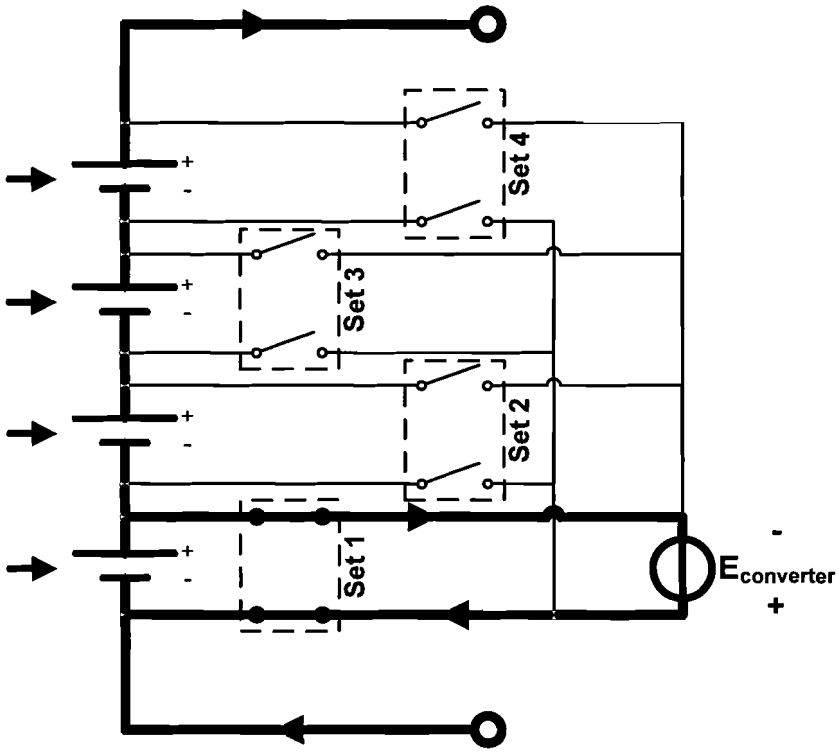

Figure 2-16: Switching scheme of the relay circuit.

2.8 Converter implementation, tests and results

The converter and its additional circuitry have first been built on test-boards. Based on the experiences with this setup, some modifications have been made, which are incorporated in the design steps discussed earlier. The final converter, including the measurement and driver circuitry, is implemented on a custom made PCB. The low-pass anti-aliasing filters are implemented on a circuit board and the relay circuitry on a separate PCB. A picture of the final circuit is shown in Figure 2-17. A 10V power supply should be connected to $V_{in}(+) - V_{in}(0)$, separate 12V power supplies should be connected to the indicated connectors, $V_{out}(+) - V_{out}(0)$ indicate the output terminals of the converter and the remaining connections indicate the outputs of the measurement circuits and the inputs for the gate drivers.

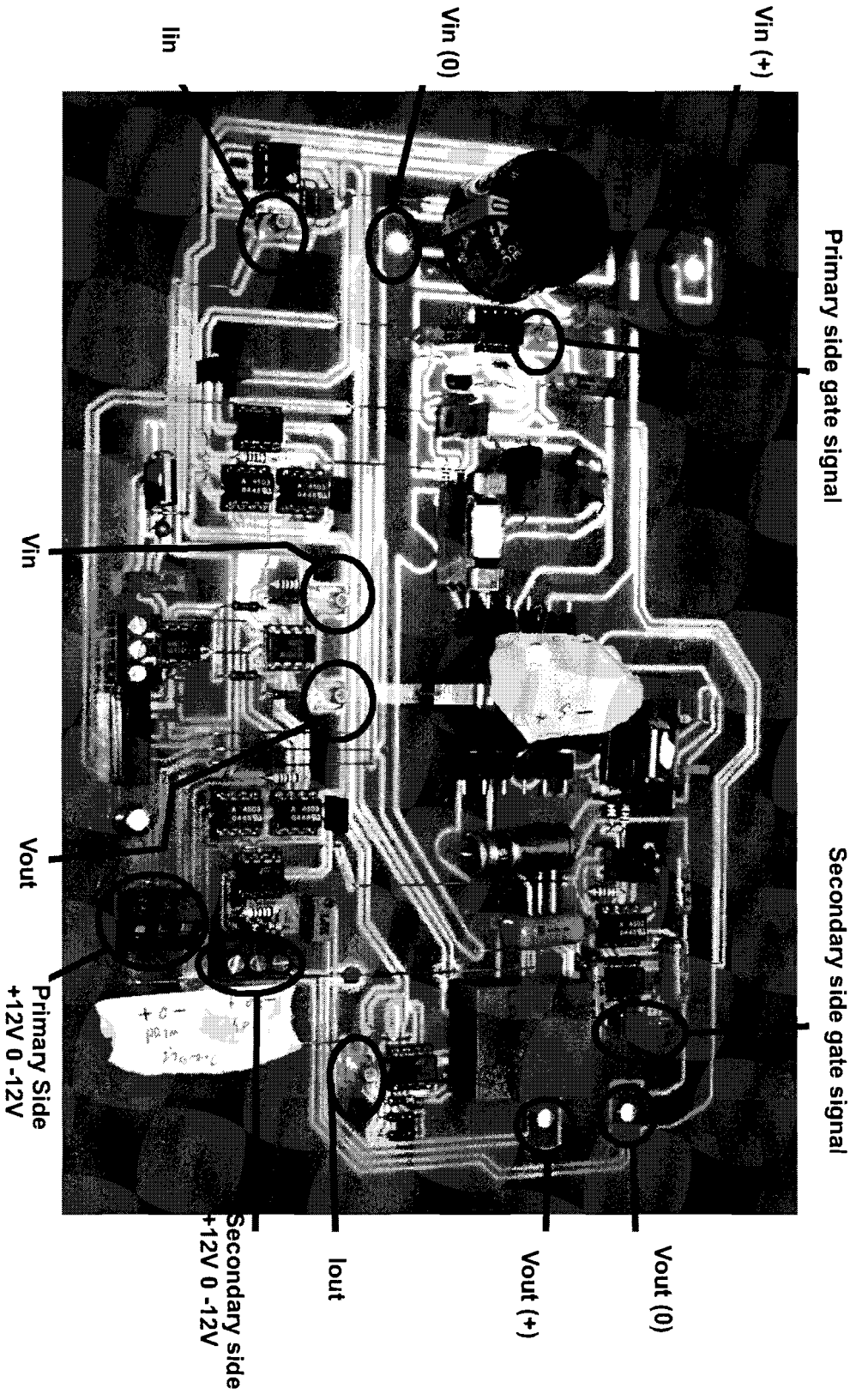

Figure 2-17: Isolated fly-back converter with its measurement circuits

2.8.1 Converter testing methods and results

In order for the converter to work, several sub-circuits should be tested during assembly. The first circuits to be built and tested are the gate drivers and snubbers. Tests of conducting paths should be enough for the latter circuit. The gate-driver has slightly different characteristics, depending on the load of the circuit or its power state. This can be seen in Figure 2-18. The lower characteristics are recorded after the circuit was completely built. The black line corresponds to a load of 5Ω and the grey line to 1.7Ω.

Furthermore, the LEM sensors, MOSFETs and the transformer should be placed on the PCB to ensure conductive paths on the primary and secondary sides of the converter. Testing of the fly-back converter is done with resistive loads of 5 Ω and 1.7 Ω. This gives the possibility to use the standard duty-cycle of 0.5 of the used function generator. The combination of this load and the duty-cycle will provide a not too high power output.

The snubber is checked by measuring drain voltages. If any disturbing oscillations still exist, the snubber has to be redesigned. Oscillations did occur at first. Damaged snubber capacitors, probably due to high currents, were the source of these oscillations. This problem has been solved by placing 22.3nF and 33.3nF capacitors in parallel. This reduced the voltage overshoot slightly more and solved the peak-current problem as it is now levelled over two capacitors.

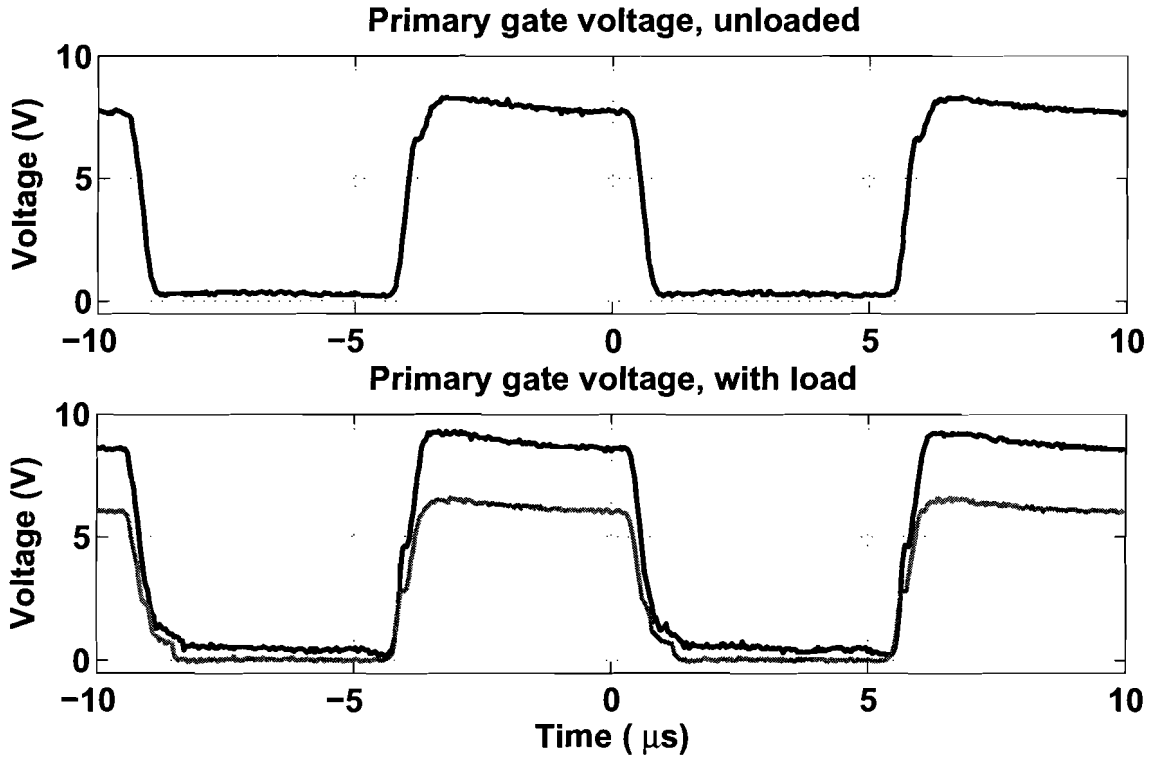

Figure 2-18: Primary V_{gs} with the power circuit turned off (top) and with two different kind of loads (bottom)

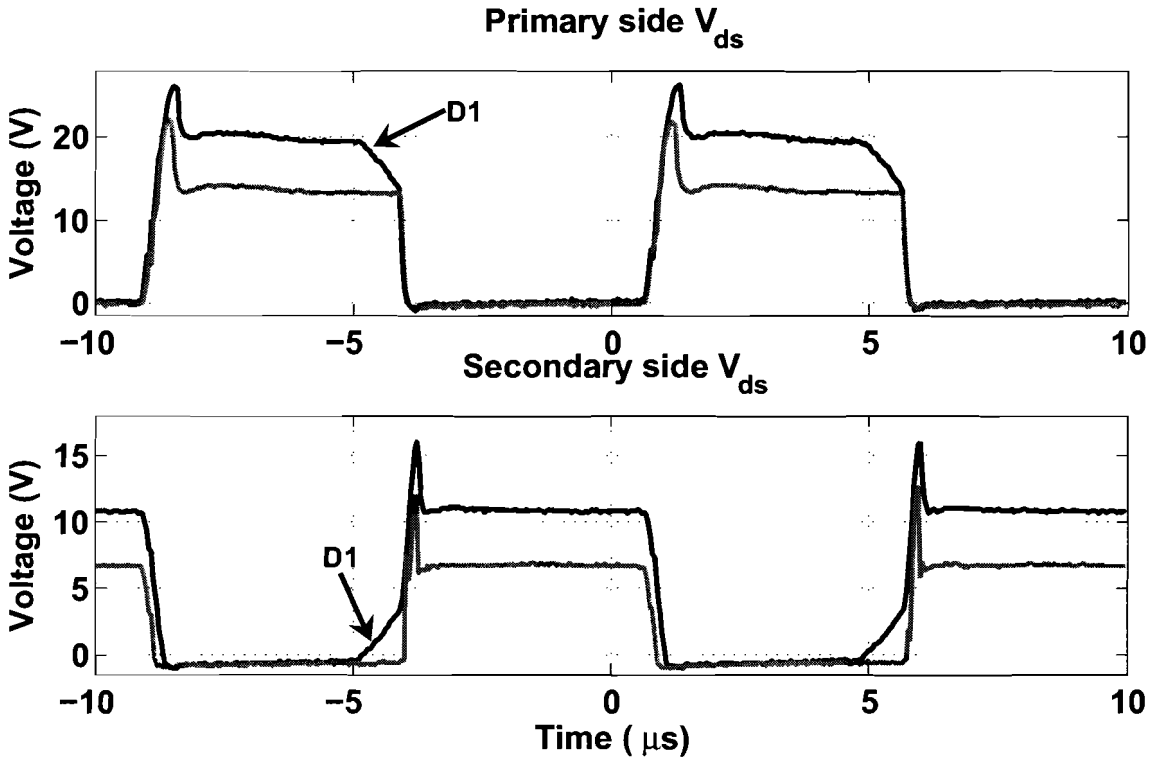

Figure 2-19: Primary and secondary drain-source voltages of the MOSFETs

The currents through the secondary snubber capacitor were not as large as on the primary side, causing no failure. It was however replaced by a slightly larger model, as it heated up. The resulting drain-source voltages for the different loads are shown in Figure 2-19.

Finally, the measurement circuits are constructed. These circuits must be able to measure the low frequency (<1 kHz) behaviour of the in- and outputs. The anti-aliasing filters will cut-off anything above 5kHz. The linearity check and calibration graphs for the voltage measurement circuits can be found in appendix C.2.2.

Besides the difference in voltage levels between the 5Ω and 1.7Ω load waveforms, another difference is shown in Figure 2-19, indicated by D1. The converter is operating in discontinuous mode when it is loaded with a 5Ω load. This means that the energy in the transformer has been completely transferred to the secondary side during $(1\text{-}D)T_s$. As a result, the secondary side snubber capacitor as well as the parasitic C_{ds} of the secondary side MOSFET is charged by the output capacitor, causing the slope visible at D1.

2.8.2 Output characteristics for different loads

The output characteristics of the converter are recorded with the oscilloscope (See Appendix D). The top graph of Figure 2-20 shows the signal for a 5Ω load measured directly at the scope. The straight dotted line shows the response of the measurement circuit. Averaging the first

waveform with Matlab, shows that the measurement circuit represents this average quite well. The difference is probably due to calibration error. The second graph shows the output voltage for a 1.7Ω load. The effect of the secondary snubber is much more visible in this situation.

2.8.3 Output power characteristic

Relationship (2.10) shows that the output voltage of the converter is related to the duty-cycle. Therefore measurements have been done to show the relationship of the output power and the duty-cycle (Figure 2-21). These measurements have been done in two situations. First, the primary MOSFET is switched and the secondary MOSFET is turned off, thus only using the anti-parallel diode and the zener-diode. Second, both MOSFETs are switched inversely. The used topology causes a delay between the reaction of the primary and secondary MOSFET gate voltages. This ensures that both MOSFETs are not on at the same time when the primary MOSFET is switched off. However, the delay causes a simultaneous on-state at the moment of primary turn-on, which increases the efficiency at higher duty-cycles, but decreases the efficiency at lower duty-cycles, as is visible in Figure 2-21. The absolute difference between the two situations is only 0.82W in favour of the situation with both MOSFETs switching. The maximum power is also dependent on the state of the converter: it will be slightly higher at a cold start-up than when the converter has been operating for a while and has warmed up. The source used for these measurements can supply a maximum of 50W. The decline in power for $D > 0.6$ is caused by the current limiter of the source.

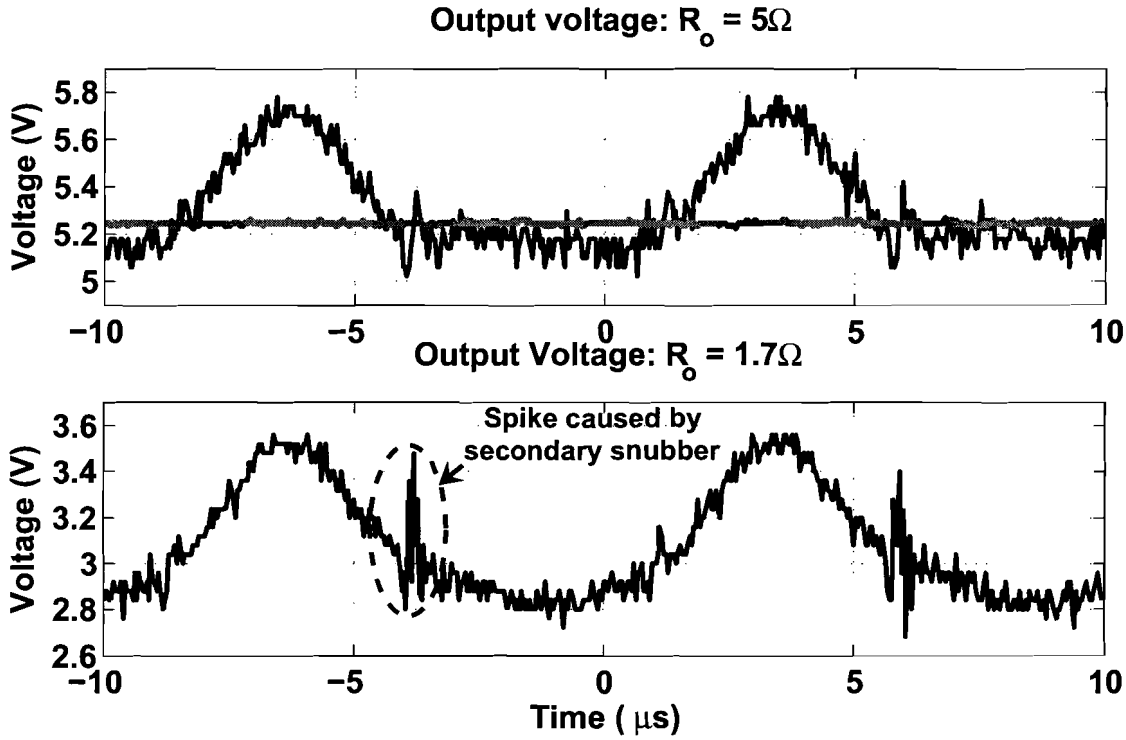

Figure 2-20: Output voltage characteristics of the converter.

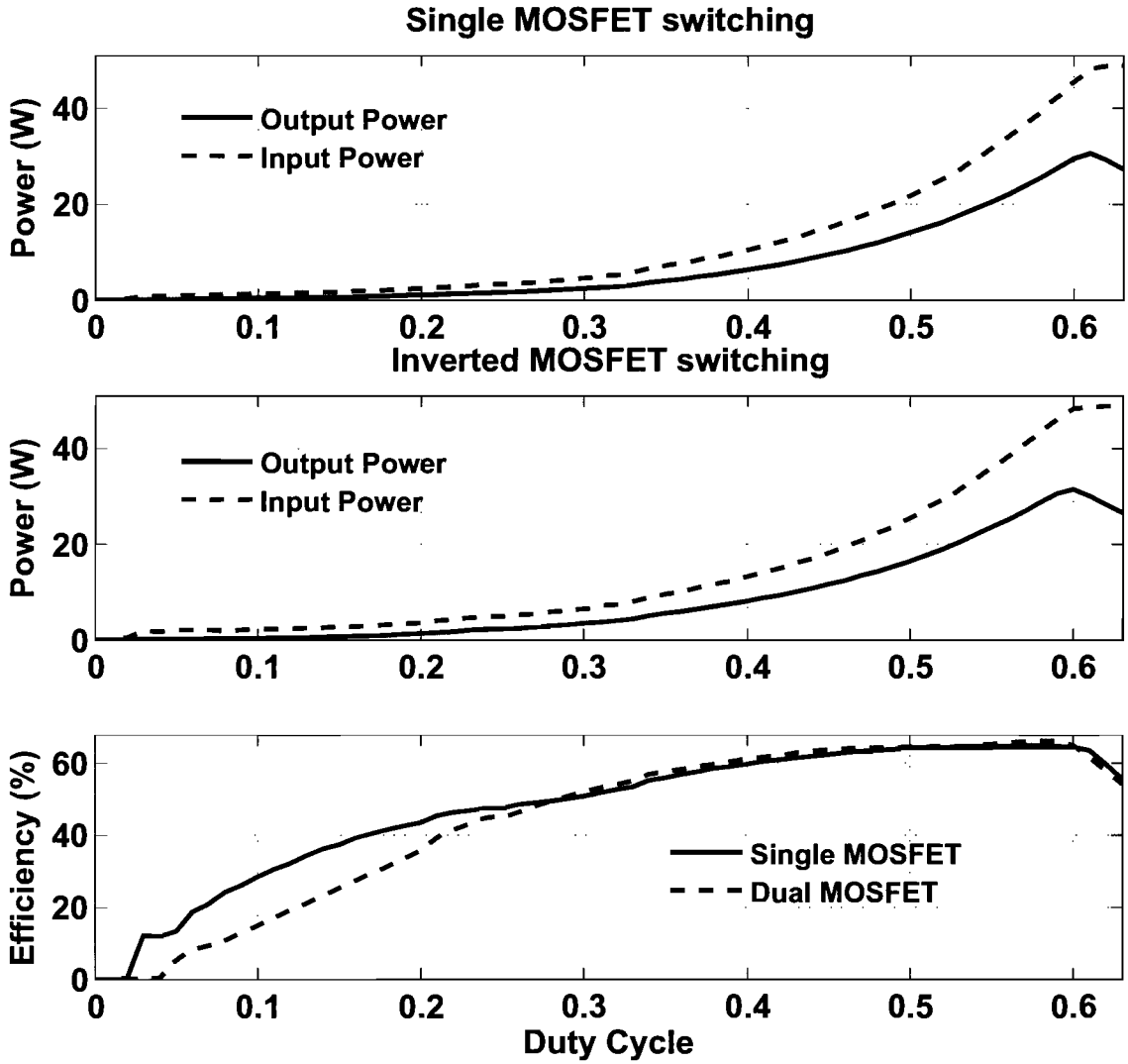

Figure 2-21: Performance characteristics of the fly-back converter

2.8.4 Reversed converter operation

In order to minimise the amount of current that will be flowing through the relay switches at turn-on and turn-off, the converter output needs to be shorted. The current drawn at such a moment, will be similar to the pulsing technique described in the introduction, with the exception that the pulse is not adjustable in amplitude. The energy going through the converter at this time can be transferred to the primary side. The source at the input must be able to cope with this for brief periods of time. The low efficiency of the converter can also be useful on this regard, as some of the energy will be dissipated before the input of the converter is reached.

A test was done to check the ability of the converter to feed back energy. This was done by placing a Øltronix voltage source (EM1473, see Appendix D) at the output of the converter. The

result is shown in Figure 2-22. The source at the input must be taking in energy, as the voltage on the input capacitor (V_{in}) is not increasing rapidly. These results indicate that feeding back energy is possible with the current set-up.

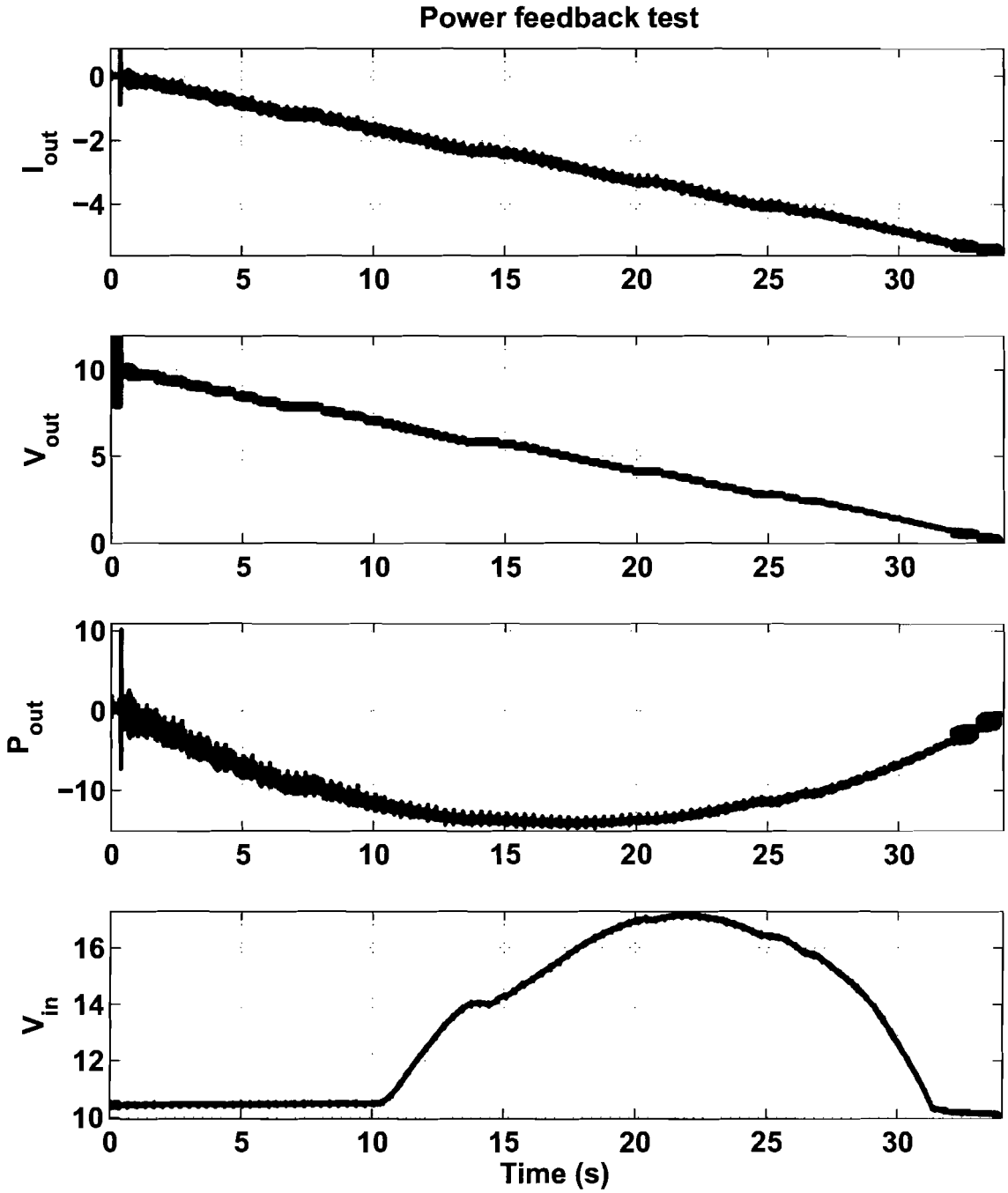

Figure 2-22: Power feedback test results

3 Fuel cell regeneration

The converter is connected in parallel to the fuel cell via a four sets of two relays, as is described in section 2.7.1. and is shown in Figure 2-16. The converter voltage must be made as low as possible at the time of switching, to prevent large peak currents during switching. This means the converter should be controlled by the output voltage controller set to 0V. After which, the controller is switched to the cell voltage controller and the desired pulse shape is made. The controller is then set back to 0V, a switch to the output voltage controller is done and the relays are switched again. A possible benefit of this switching technique is the creation of additional water in the cell before and after applying a pulse, reducing the risk of dehydrating the fuel cell with a regeneration pulse.

The gas used for the CO poisoning tests is a simulation of gassified biomass. Such a gas is often referred to as synthetic gas or "syn-gas". The syn-gas used for the CO poisoning measurements contains 30ppm CO and the complete specification is given in appendix E.

A linear load, consisting of five power MOSFETs controlled by a PI controller in dSpace, is used as the adjustable load for the fuel cell cartridge.

3.1 The measurement setup

The measurement setup is shown in Figure 3-1. The converter or voltage source is connected via relays to a PCB with sets of MOSFETs placed in parallel to each cells. These MOSFETs are used to short circuit the cells every now and then to humidify the membranes. Two have been put in series, as the diodes would otherwise short circuit the applied voltage source when voltages lower than their (anti-parallel diode) thresholds are applied. The cell voltages are also measured on this PCB. A direct consequence of this is that the actual cell voltages will be lower than measured as soon as the voltage source supplies current. Furthermore, during negative pulses, the sum of the cell voltages is not to get below the threshold voltage of the diodes in the linear load, as this will reverse the polarity of the current. Finally, the linear load is used to draw a current from the cartridge as desired.

Figure 3-1 only shows the MOSFETs, relays and measurement points for cell 3. The actual setup has the shown circuit for each cell. There is only one source\converter and only one linear load.

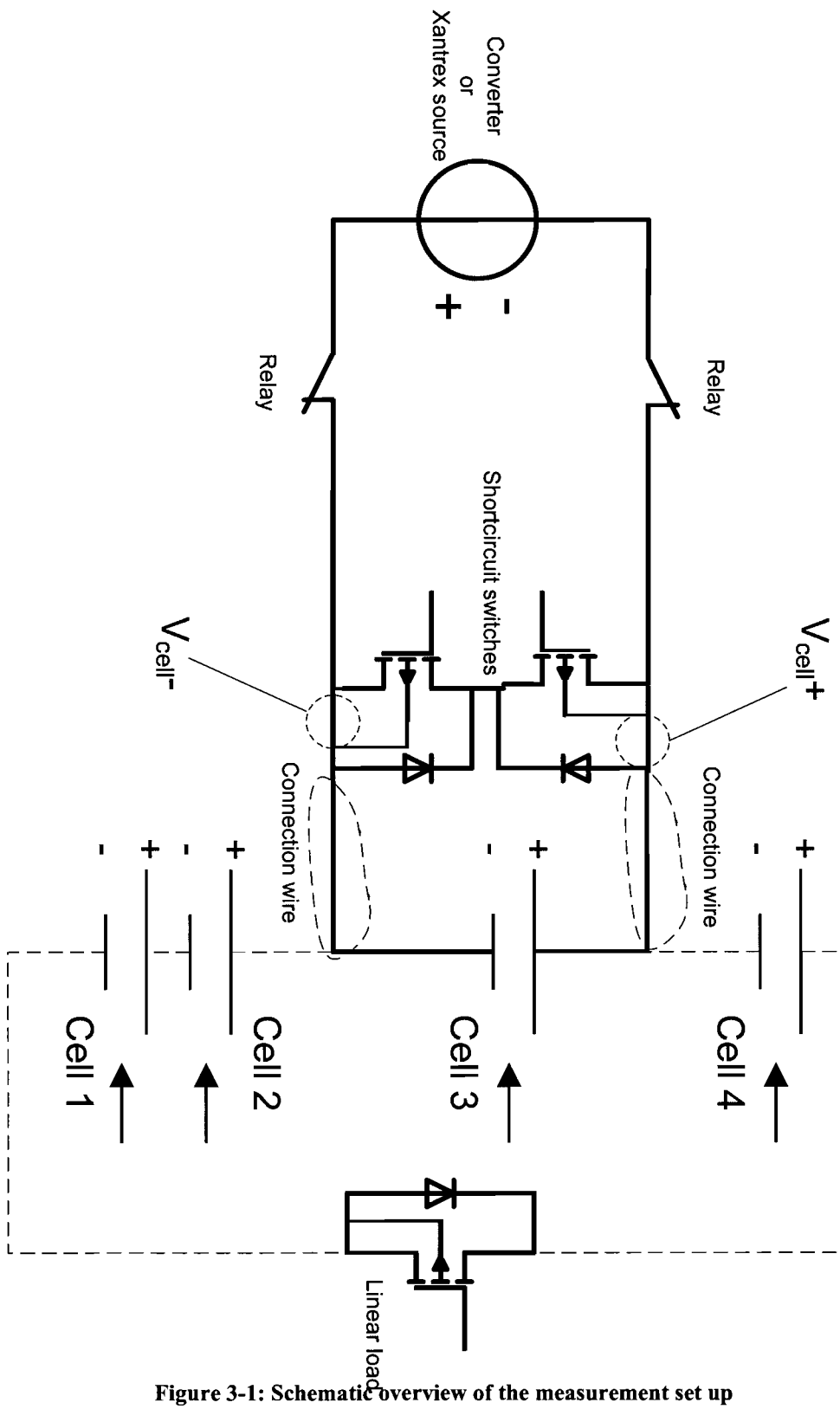

Figure 3-1: Schematic overview of the measurement set up

3.2 Reversing polarity

First, a test was done to check whether the converter could reverse the polarity of the output of a voltage source. The test was successful. Second, short circuit tests were performed with the fuel cell. One test used equal polarities of the fuel cell and the output of the converter. Another test used opposite polarities; both tests were successful. After these tests, reversing the polarity of the fuel cell was tested.

It was attempted to reach cell voltages lower than -2V by lowering the cell voltage with a negative slope. However, the current protection interrupted the measurements, in order to prevent damage to the converter, before the end of the slope. Different slopes and pulses have been tested to see whether or not the shape of the slope had an effect on the necessary current drawn. The conclusion was that the used combination of input voltage and input current was not sufficient. Therefore, the input voltage was increased to 15V, this did not solve the problem; the current protection still interrupted the measurements. Then, the input source was replaced by a more powerful one (Xantrex source, Appendix D). The new source provided the ability to reach a lower cell voltage. However, it was still not possible to reach values lower than -2V.

3.2.1 Volt•Second mismatch

The only remaining explanation for the necessary high input currents is a saturation of the fly-back transformer. It was found that the volt•second products of the primary and secondary converter sides did not match. The basic principle of the fly-back converter is that the energy stored in the transformer during one switching cycle is also released during the same cycle. With a fixed magnetising inductance, the product of the voltage over this inductance and the time this voltage is applied is a measure of the energy put into the transformer. In this case, the product of the primary side is larger than that of the secondary side. As a result, energy will be built up in the transformer, causing saturation. Figure 3-2 shows the saturation of the transformer. In order to clearly identify saturation, the switching frequency was lowered to 10kHz. The current at which the effect of the saturation becomes apparent, is found to be 24A. This is higher than the value calculated in (2.19). This is most likely due to the conservative value for B_{max} chosen during the design of the converter.

The solution to this problem is using a variable frequency control of the converter and if necessary, a redesign of the transformer. As an alternative, the Xantrex source is used for the desired measurements. To acquire the proper boundary conditions for a new converter, the voltage-current characteristic is measured.

3.2.2 Voltage current characteristics

The voltage-current characteristic is made by switching the relays and immediately afterwards applying a negative slope to the cell voltage controller, as is shown in Figure 3-3. This figure shows a connection between cell voltages. Every time a negative voltage is applied to cell 1, cell 2 will respond linearly and the same applies for cell 3 and 4. The linear relationship that describes this effect is found to be

$$V_{coupled} = \frac{I_{source}}{42} + 0.85V. \tag{3.1}$$

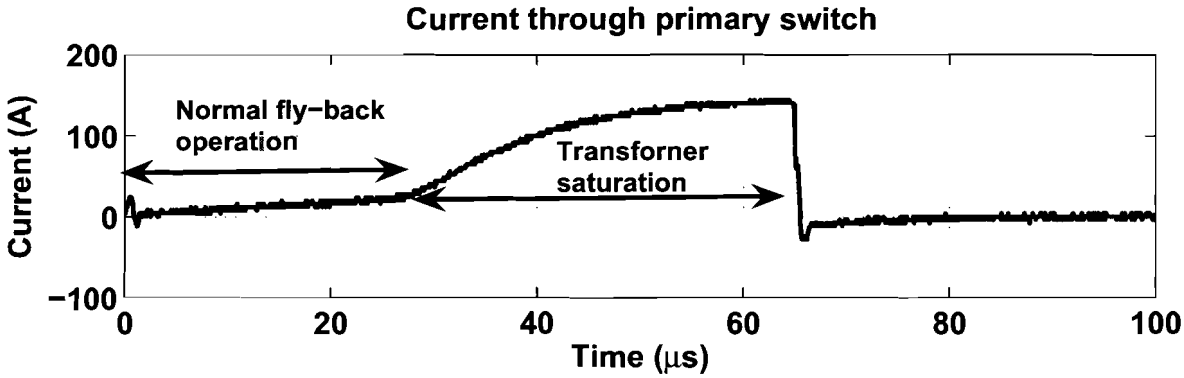

Figure 3-2: Transformer saturation due to a volt*second mismatch

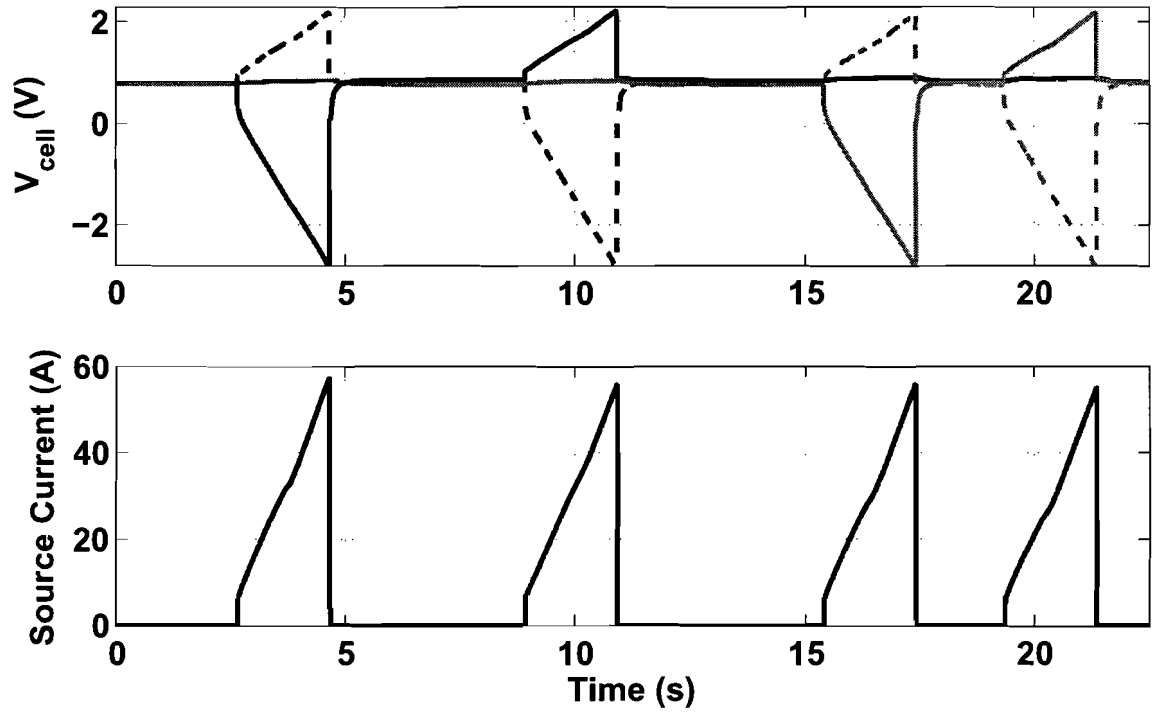

Figure 3-3: Data from which Figure 3-4 has been derived, (-) = $V_{cell}1$, (--) = $V_{cell}2$, (-) = $V_{cell}3$ and (--) = $V_{cell}4$

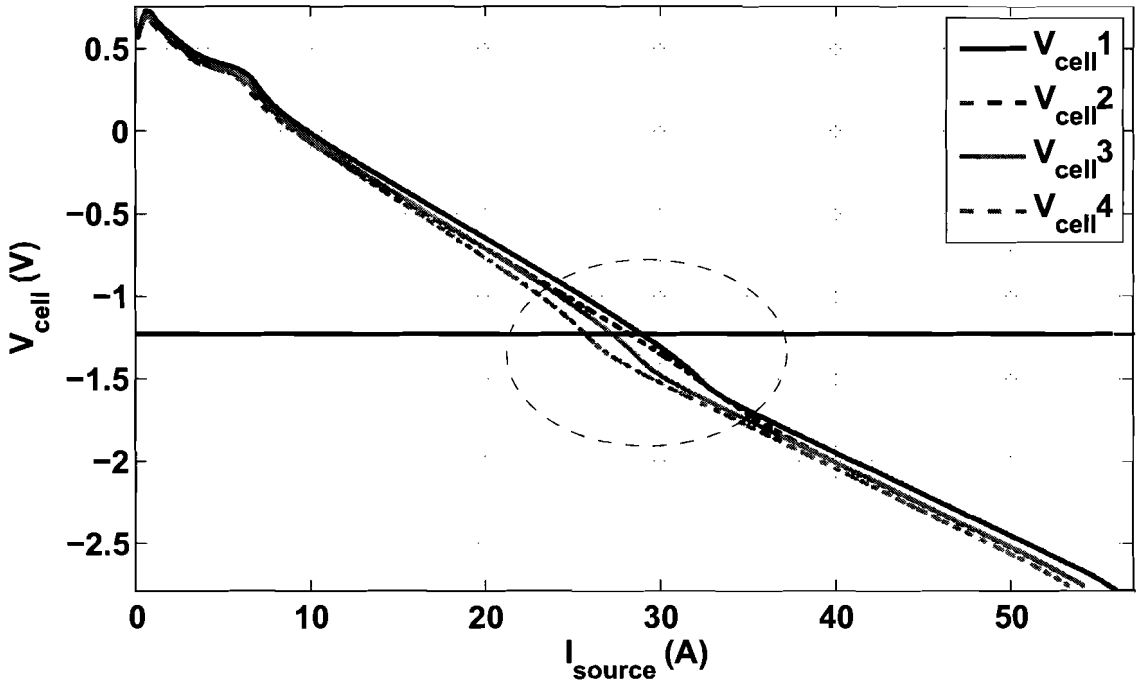

Figure 3-4: Voltage Current characteristic for a fuel cell in reversed polarity

A positive increase of a cell voltage can have several known causes. First, a reduction of the load current brings the cell in a different state and increases the cell voltage. As the (stack) load current is zero during these measurements and the raised voltage is well above the theoretical limit of a fuel cell, it is unlikely this is the case. Second, the voltage can increase if a negative current is forced through the cell. The voltage source is placed in parallel with just one cell at the time and with a reversed polarity. Therefore, no conductive path exists to cause a negative current through the adjacent cell. The remaining possibilities are an error in the set up, the influence of the cartridge or an electrochemical effect.

Figure 3-4 shows the current voltage characteristics gathered from the data of Figure 3-3. The non-linear behaviour below 7.5A is due to the behaviour of the source and the fuel cell right after the start of the measurements. Neglecting the low-current behaviour, the slope starts off linearly. The horizontal line indicates -1.23V, the voltage required for the reversed fuel cell reaction (1.6). Non-linearities are clearly visible around this voltage, indicated by the circle. A steeper slope with respect to the current follows after these non-linearities. This could indicate the reverse fuel cell reaction is taking place, which is as expected.

3.3 CO poisoning

It is assumed that the individual cells in a fuel cell cartridge are placed in series with respect to the fuel flow. As a consequence, the hydrogen content of the fuel gas will decrease as the gas goes through more cells. This means that the last cells will have to deal with a relatively higher amount of CO and will be poisoned first and faster. Furthermore, by increasing the load of the cartridge, the hydrogen will be consumed more quickly, causing a more rapid poisoning, assuming that the flow remains constant. Finally, the rate of poisoning can be increased by reducing the flow of the gas. This will prolong the time each gas molecule stays in the cartridge.

A measurement is done to determine the effect of CO on the cell voltage. It is repeated seven times to determine whether the poisoning of cells is a predictable process. The results are shown in Figure 3-5. Measurements 3 to 6 show very similar results as measurement 2 and are shown in Appendix F, Figure 6-11. During these measurements, the fuel cell is fed with syn-gas and the linear load is turned off at first $(t < 20s)$. After that, the load is set to 6A, until the voltage over cell 2 has reached a value of -1.05V. This cell is chosen because test measurements have shown that this cell is affected most by CO, resulting in a negative voltage. The voltage of -1.05V is chosen because the voltage did not change during test measurements.

Figure 3-5 shows the degradation of the cell voltages of cells 1 and 2. As cell 2 gets poisoned, the hydrogen reaction decreases. This translates into a lower cell-voltage, till no voltage is generated at all. At the same time, the other cells still provide enough voltage to deliver power to the load. The current forced through the poisoned cell causes a voltage drop over its internal impedance, causing a negative voltage to appear over the cell. Each subsequent subfigure of Figure 3-5 and Figure 6-11 are chronological. The data of measurement 1 shows a longer delay before poisoning occurs compared to the other measurements. This can be explained by a longer rest time (no load) before the first measurement starts. Each subsequent measurement has an equal rest time between load changes. The rise of the cell voltages of cell 3 and 4 are caused by a decrease of the load current, as can be seen in Figure 3-5, due to a lower stack output voltage. The last measurement did not go as expected, as the cell voltage did not reach the switch-off criteria. An interesting effect can be seen in the data of measurement 7; oscillations start to occur about 90 seconds after the load change.

The data presented in Figure 3-5 indicates that periods of no current through the cells have a regenerative effect as the measurements were done sequentially. Only 20 seconds of data is absent between two sequential measurements (which equals a time of 70 seconds between load changes.). Preliminary tests have shown that pulsing the load can be beneficial.

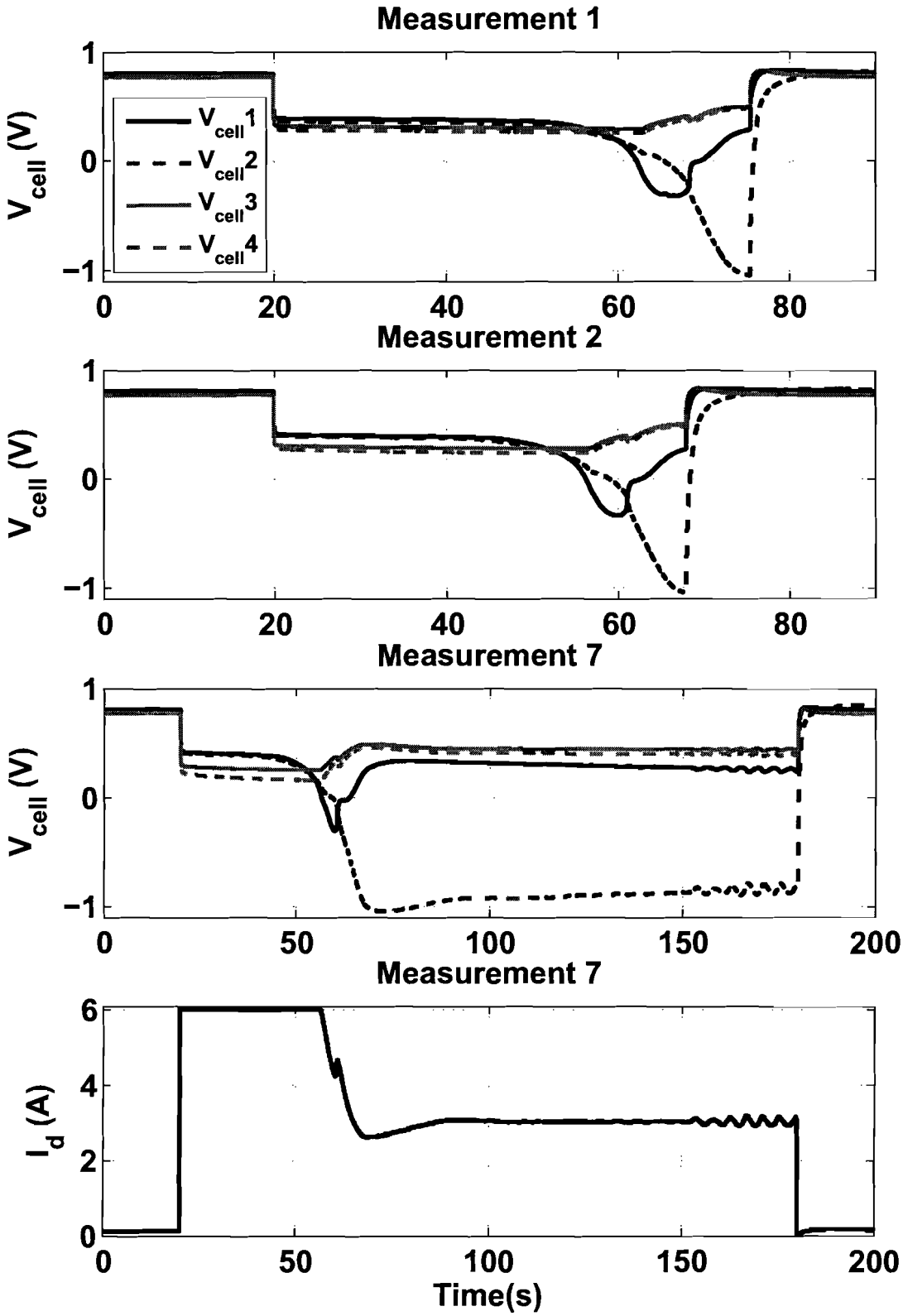

Figure 3-5: Poisoning of the fuel cell stack at 6A load

3.4 Pulsing with negative voltages

When electrolysis is taking place, an increase of voltage will only result in higher currents. More charge means more production of gasses. The pulse shape will be a trade-off between pulse amplitude and pulse width, as both parameters control the amount of charge supplied to the electrolysis reactions. It is expected that the pulse amplitude will be limited by a saturation level; there is only a limited amount of water present near the electrodes and it takes time for more water molecules to get to the electrodes. The current voltage characteristic of Figure 3-4 indicates that at a voltage of -1.7V the fuel cell behaves linearly, thus, this voltage is taken as a minimum amplitude for the regeneration pulse.

A range of pulses of different width and frequency have been tested to find an indication of regeneration. Most tests concerning frequency or timing in general had a pulse width of 0.5s and amplitude of -2.5V. The pulses did not have a regenerative effect on the poisoned cells 1 and 2. Finally, measurements have been done to see whether or not a pulse shifts the time at which a cell's performance degrades severely.

Notes of interest for the measurements done in the following sections are given in Appendix F.

3.4.1 Timed pulses on cell 2

A series of measurements is made which start with a reference, that is, without a pulse. After that, the time at which a pulse is executed is varied between measurements. Each pulse happens at a pre-defined time.

The first timed test revealed a deterioration of cell 4. This can be seen in Figure 3-6; the voltage drops to zero whereas this did not happen with the measurements of Figure 3-5. It was assumed the cell was damaged somehow, as cells 3 and 4 have not shown signs of pollution in the past. Furthermore, similar behaviour is observed with cells in different cartridges not long before they did not respond at all anymore, while being fed with pure hydrogen. Figure 3-6 shows the voltage drops a lot quicker than before after the load is applied. The oscillations on the voltage of cell 2 are also visible again.

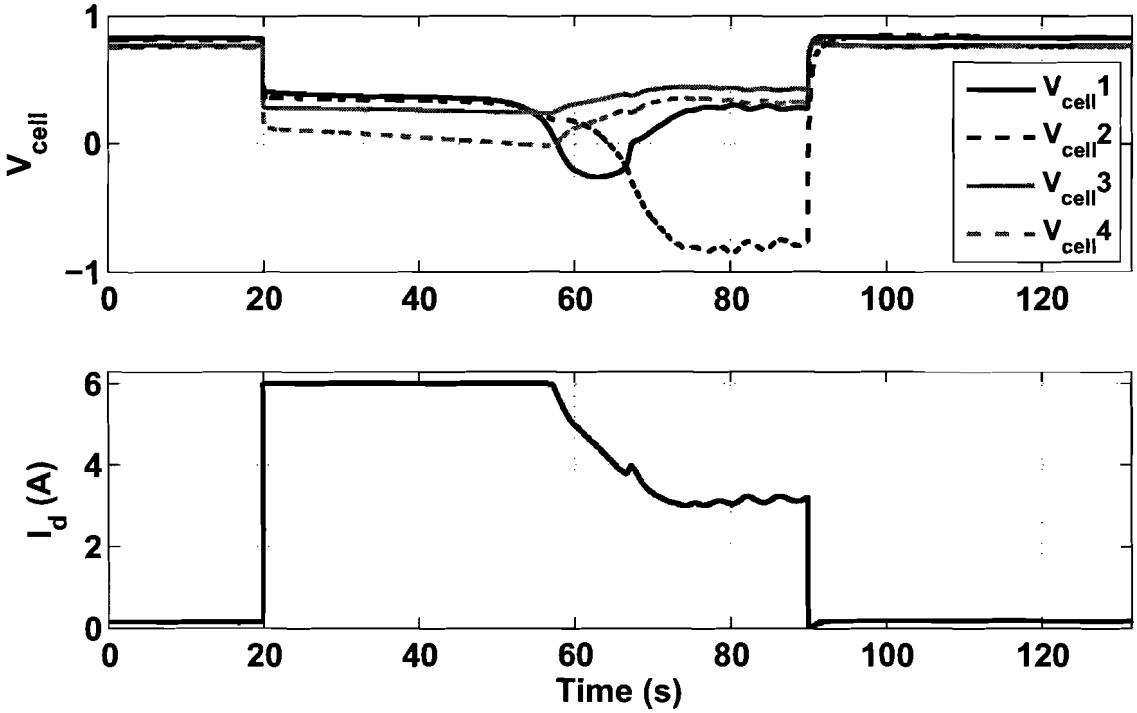

Figure 3-6: Deteriorated voltage of cell 4

Preliminary tests showed better performance of cell 4 at a load of 3A. However, the time of poisoning cell 2 was found to be too long to do the desired measurements. Therefore, a load of 4A was chosen.

The results of the 4A measurements 1 to 5 are shown in Figure 3-7 and Figure 3-8 and measurements 6 and 7 are shown in Appendix F, Figure 6-12. Several times the poisoning occurred sooner than expected, causing a pulse to be generated after the load was already turned off or during the time during which cell 2 is negative. These datasets have also been included to preserve the chronological order of events, which show developments of certain phenomena. Furthermore, the voltage range displayed is limited to see the effect of a pulse, not the pulse itself.

The figures clearly show that $V_{cell}4$ starts oscillating after being negative for 30 seconds. This specific pattern has also been found in literature **[13]** and is referred to as sustained potential oscillations or "self-oxidation". Thomason et. al. mention this effect is made possible due to the low oxidation potential created by the Ruthenium catalyst they are using. This makes the oscillations observed here special. Apparently, this phenomenon can also occur in fuel cells utilising Platinum-only catalysts. The difference with the oscillations observed in literature is that those voltages remain positive, whereas these require a negative voltage. Furthermore, this means the cells are not damaged and that a measurement with a load of 6A can be attempted again, which has a higher rate of poisoning due to the higher consumption rate of H_2. The results of that measurement are given in section 3.3.6.

The pulses applied during this test show an increase of the cell voltage of cell 2 right after the pulse. However, the pulse also decreases the time needed for the cell to be poisoned, with respect to the first and last three measurements. These measurements have been repeated with pulses applied at the other cells to see if the results are similar.

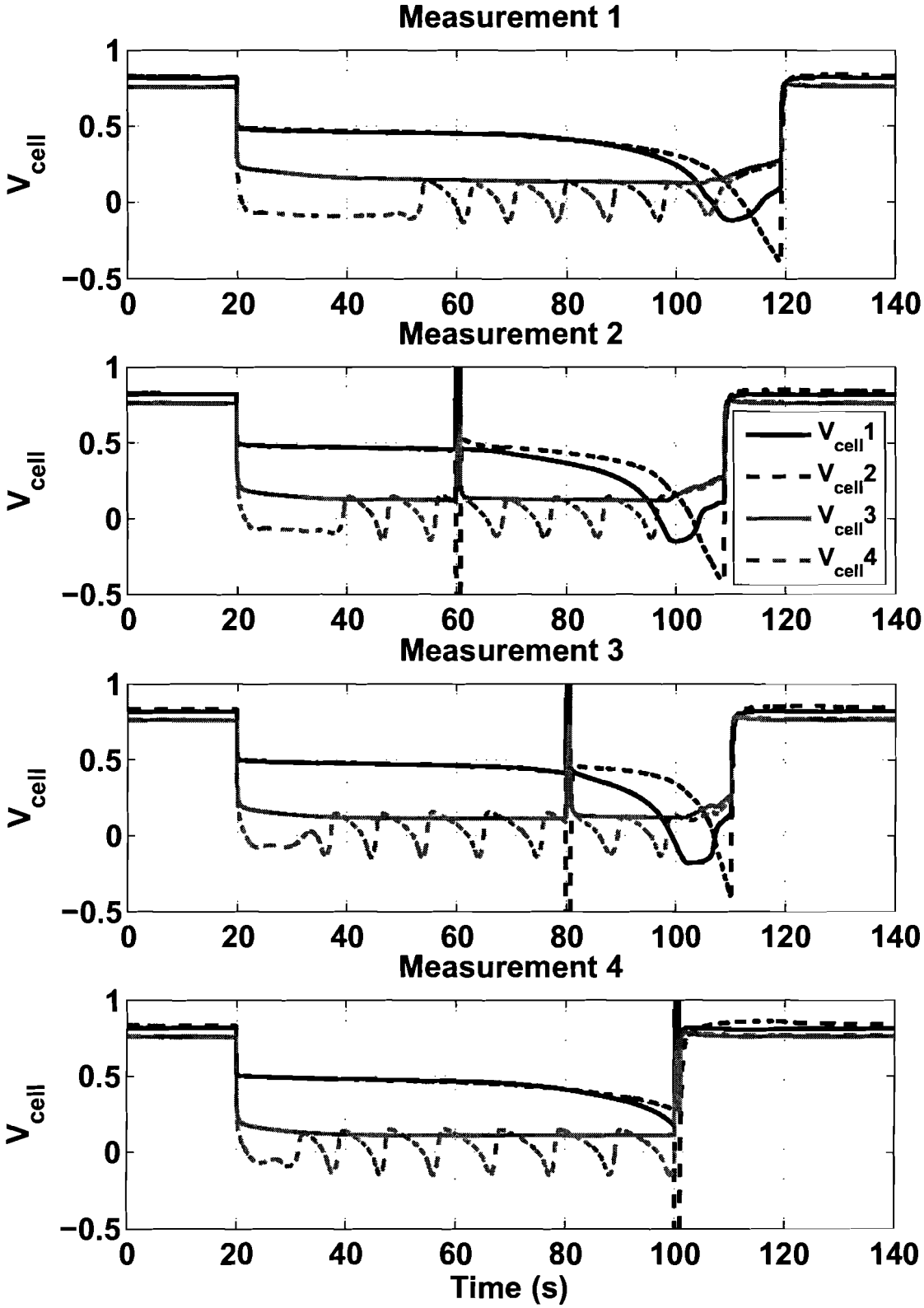

Figure 3-7: Timed pulses at t = 60s, 80s and 100s, applied to cell 2, with a 4A load

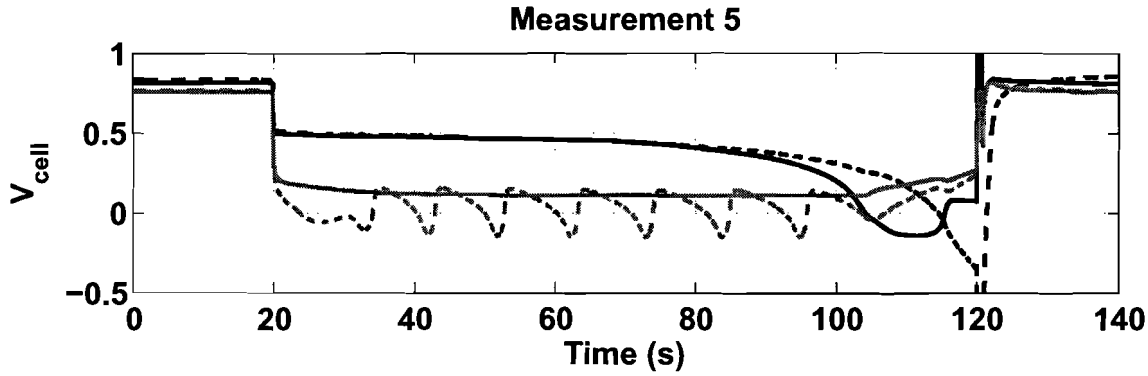

Figure 3-8: Timed pulss at t = 120s, applied to cell 2, with a 4A load

3.4.2 Timed pulses on cell 1

The time at which $V_{cell}2$ reaches -0.4V is decreased by about 20 seconds compared to the results in the previous section and the reference measurement. The second and third graph of Figure 3-9 show mixed effects of the applied pulse. The second indicates a rise of the cell voltage compared to before the pulse and the third shows a decrease of the voltage or a continuation of the slope already in progress. The data of measurements 5 and 6 are shown in Appendix F, Figure 6-13.

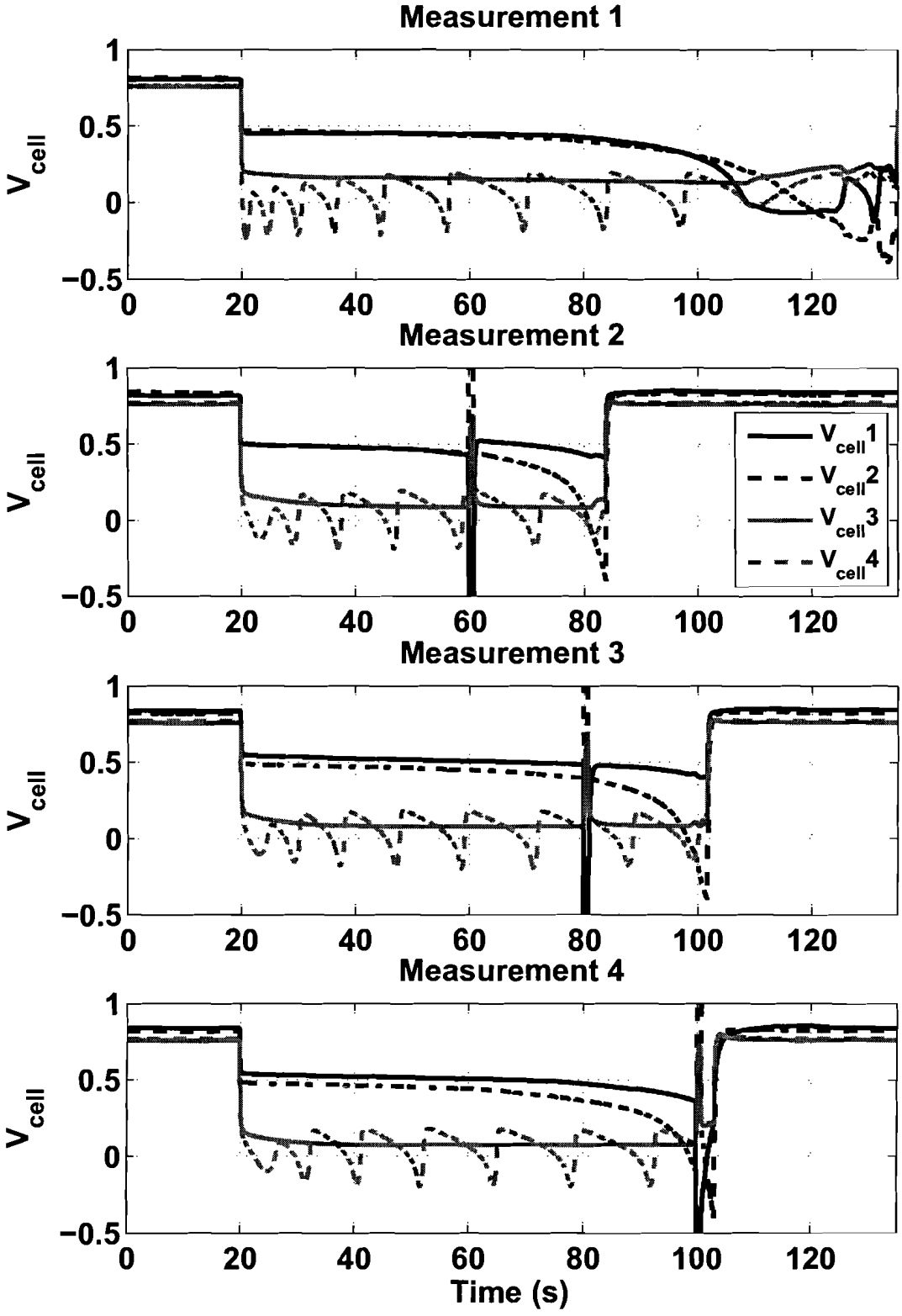

Figure 3-9: Timed pulses on cell 1 at t = 60s, 80s and 100s

3.4.3 Timed pulses on cell 3

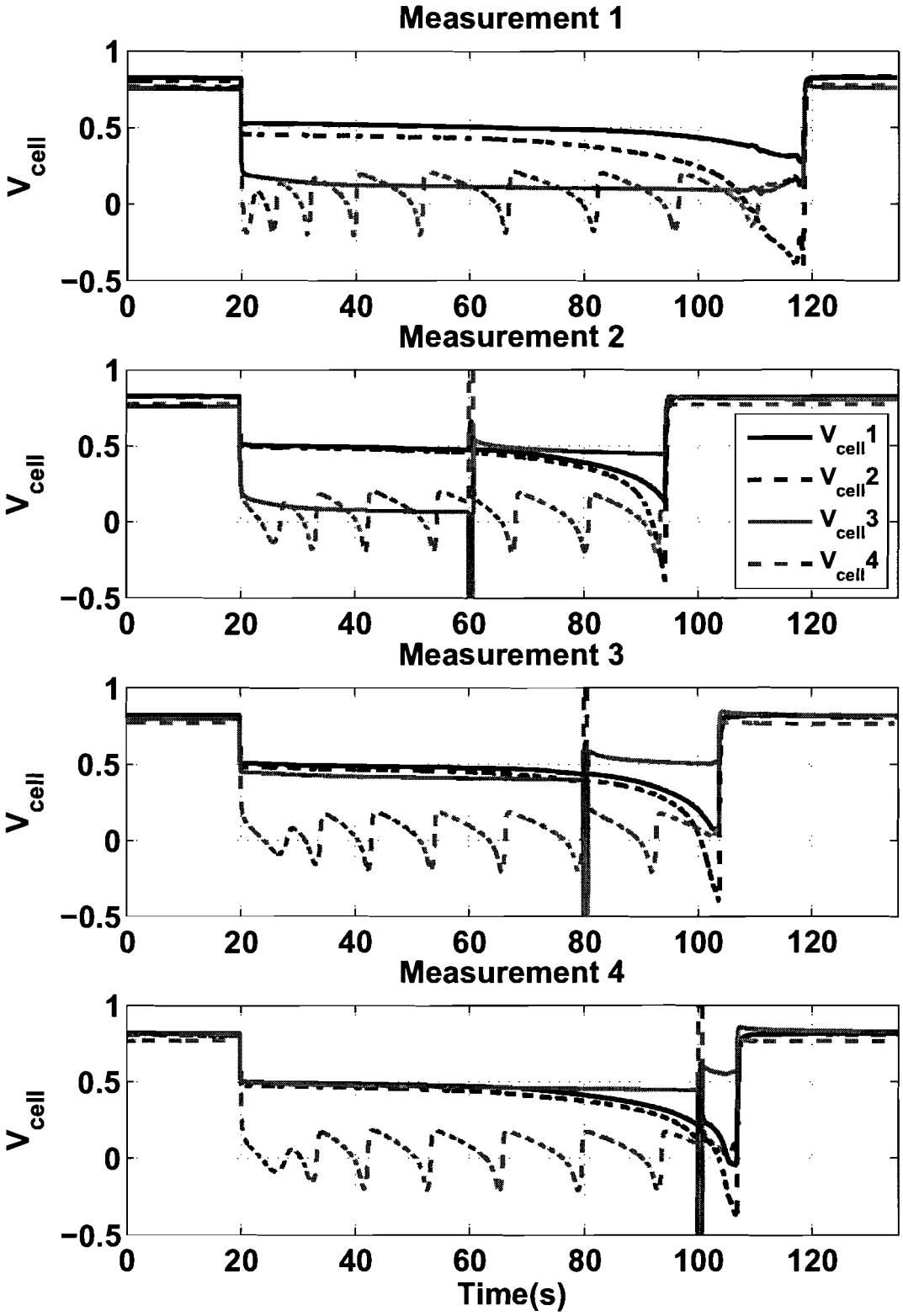

Figure 3-10: Timed pulses on cell 3 at 60s, 80s and 100s, with 4A load

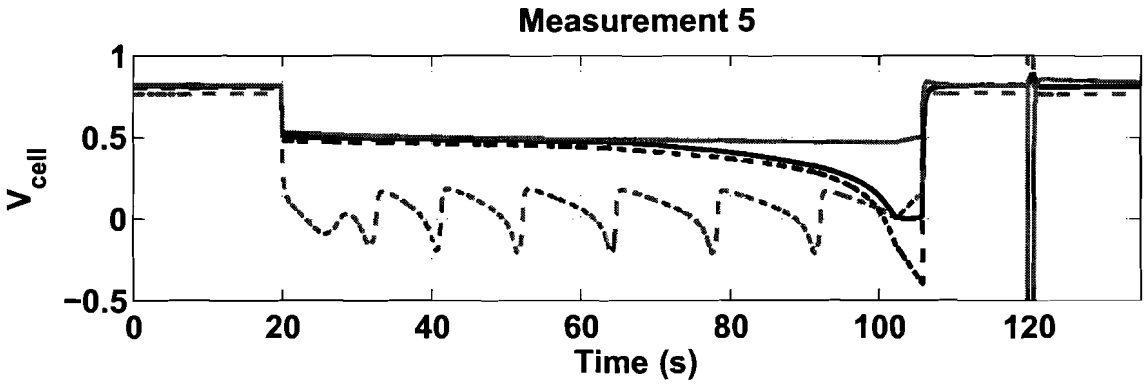

Figure 3-11: Timed pulse on cell 3 at 120s, with a 4A load

The second graph of Figure 3-10 indicates that a negative pulse has a positive effect on $V_{cell}3$. The cell is regenerated by the pulse. The positive counter pulse on cell 4 does not disturb the oscillating behaviour, nor are the other cells influenced significantly by either pulse. Each subsequent pulse increases the cell voltage of cell 3. Furthermore, it is shown in Figure 3-11 that the voltage of cell 3 remains at a high level throughout the measurement.

3.4.4 Timed pulses on cell 4

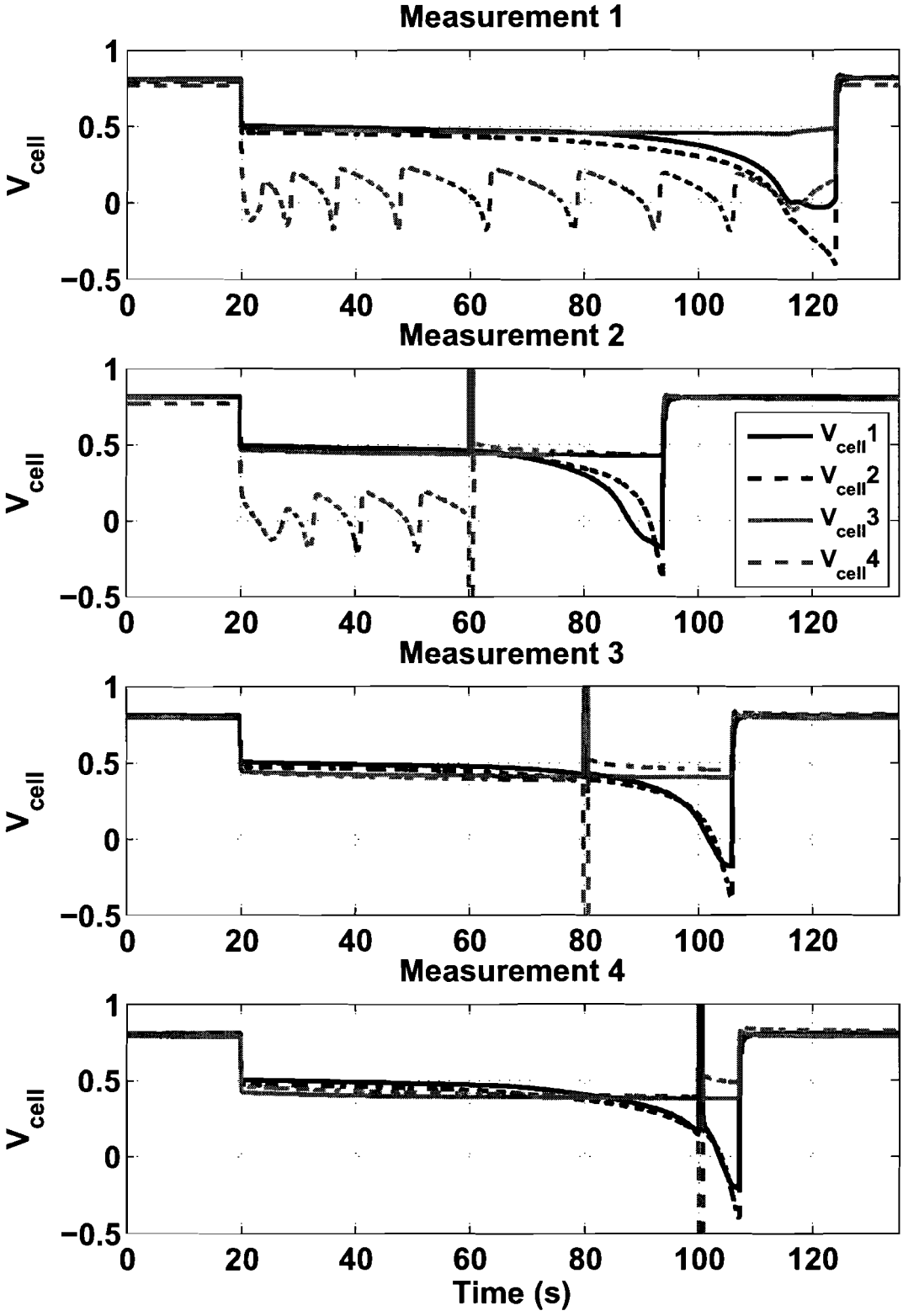

Figure 3-12: Timed pulses on cell 4 at 60s, 80s and 100s, with a 4A load

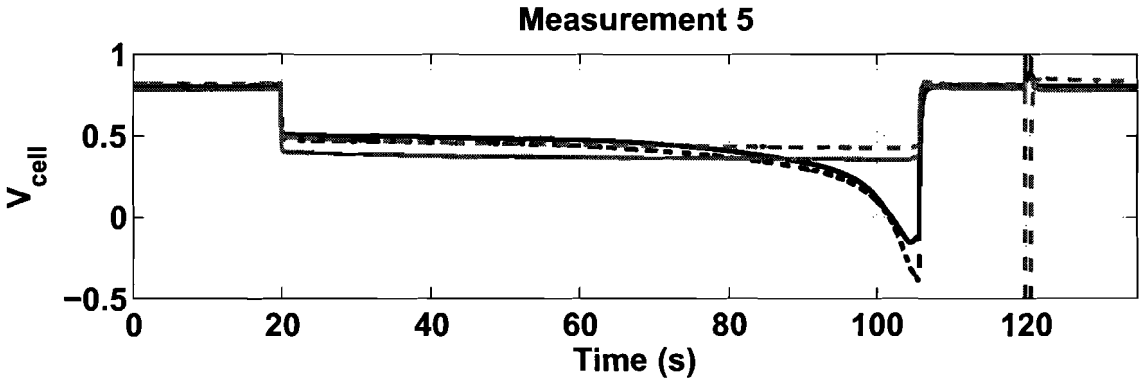

Figure 3-13: Timed pulse at 120s, with a load a 4A load

The observation of section 3.3.4 can also be made with these measurements. The pulse regenerates the cell and the oscillation is stopped. Pulsing is thus effective for cell 3 and 4 when they are hindered by CO poisoning. The data of measurements 1 through 5 also indicates a steady decrease of the voltage of cell 3. A comparison with the data of section 3.3.4 also shows that cell 4 is poisoning at a faster pace than cell 3. This most likely explains why cell 4 has reached a state of sustained oscillations and cell 3 has not.

3.4.5 Timed pulses at 6A

The reason for switching to a load of 4A was the behaviour of cell 3 and 4. As it is shown that these cells can be regenerated, the 6A measurement is done again. First, a series of four measurements is done with a pulse applied to cell 1. The data of the cell 1 and 2 measurements is shown in Appendix F, Figure 6-14 and Figure 6-15. The relevant observation is the start of the oscillations of cell 4 during the last measurement. After that, measurement series have been done pulsing cell 3, 4 and 2 respectively. The results of pulsing cell 3 and 4 are shown in Figure 3-14 and Figure 3-15. These show that cells 3 and 4 can be regenerated with a negative pulse, even with a load of 6A and that the result lasts for longer periods of time.

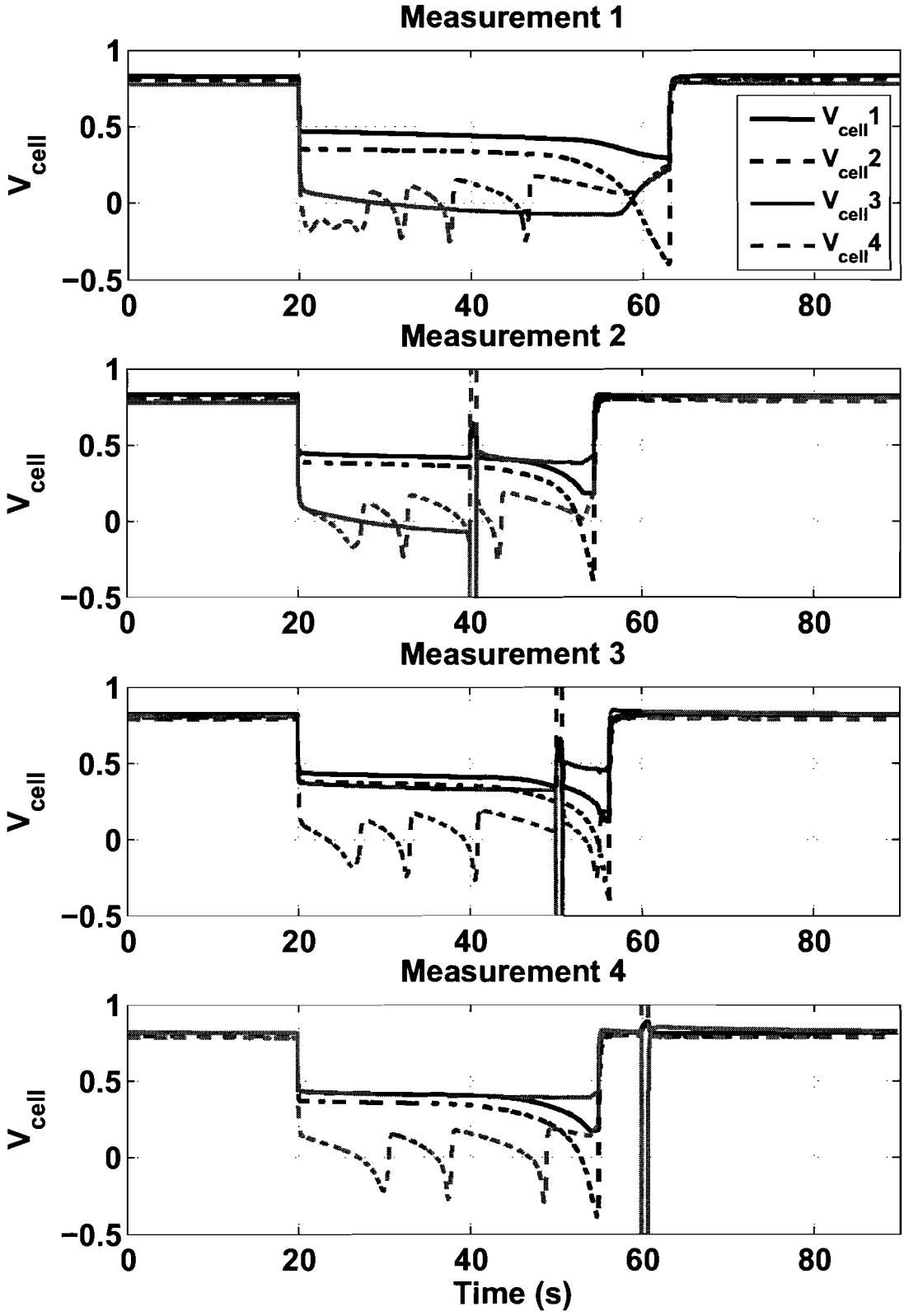

Figure 3-14: Timed pulses on cell 3 at t = 40s, 50s and 60s, with a load of 6A.

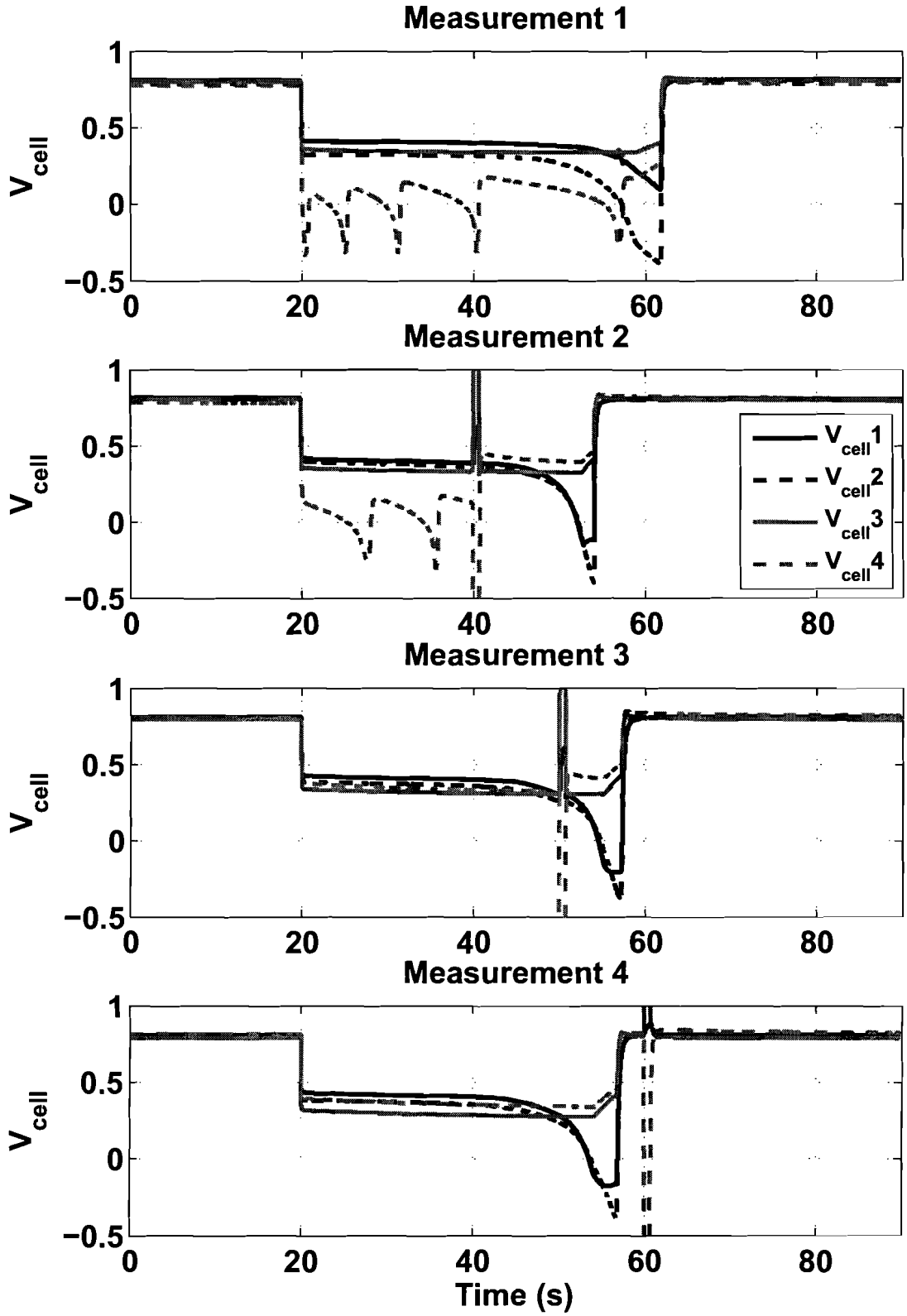

Figure 3-15: Timed pulses on cell 4 at t = 40s, 50s and 60s, with a load of 6A.

3.4.6 Conclusions and discussion

The negative voltage pulses used do not regenerate cells 1 and 2. They even increase the rate at which the voltages of these cells drop below 0V. However, turning off the load does regenerate these cells, when this is done "long enough". Cells 3 and 4 can be regenerated with a negative voltage pulse. These cells will go into a state of sustained oscillations when their poisoning level is high enough, but applying a negative voltage pulse gives a much more constant voltage response for a longer period of time. From this, it is expected a low duty-cycle low frequency pulse sequence will suffice in keeping these cells at operational levels with the used 30ppm CO gas mixture. I also suspect that the cells 1 and 2 can be kept operational for longer periods of time by pulsing their loads. This could be done by temporary redirecting the current normally flowing through the cell; by-passing the cell so it can recover or by (load) pulsing the stack as a whole.

The data presented in sections 3.4.1 to 3.4.5 also clearly show that the second measurement consequently sees a more rapid poisoning of cell 2. It is uncertain whether this is due to the pulse at t=60s or due to another effect. A consequence of this shorter poison time, is that the rest period between measurement 2 and 3 is longer than between the subsequent measurements.

The question remains which process regenerates cells 3 and 4, thus measurements of pulses with different amplitudes must be performed. If a voltage above -1.23V is sufficient for the regeneration of the cells, than the process will not be electrolysis.

It is unknown why there is this distinct difference between cells 3 and 4 on the one hand and cells 1 and 2 on the other***.

*** *More about this in Addendum 1*

4 Conclusions and recommendations

4.1 Conclusions

A converter is designed and built. It is capable to provide the 5V, 8A design specification, using a resistive load. The behaviour of the fuel cell is found to be different than anticipated, causing a volt*second mismatch in the converter, which results in the saturation of the transformer.

It has been found that negative voltage pulses do not regenerate poisoned cells 1 and 2. The only method of regenerating these cells is by making the load zero for a yet to be determined amount of time, while maintaining a gas flow through the cartridge. Furthermore, self sustained oscillations have been observed with cells 3 and 4, but at very low cell voltages. The negative voltage pulses do regenerate cells 3 and 4, causing high cell voltages for longer periods of time, with respect to the self sustained oscillations.

4.2 Recommendations

The current-voltage characteristic of the fuel cell in the fourth quadrant indicates currents of up to 60A. The output voltage needed in combination with this current has the desired cell voltage as minimum. The maximum depends on the resistance of the connection wires. A redesigned converter should be able to meet these requirements and should preferably be able to operate in at least two quadrants. This would make it possible to reduce the load for a specific cell.

More research is required to find out what causes the difference between the two sets of cells (1&2 and 3&4) and what causes them to act like sets. Also, it should be investigated how the "counter-pulse" is generated***. Furthermore, the regeneration pulse for cells 3 and 4 needs optimisation to determine what the mechanism behind the regeneration could be and to minimise the required energy per pulse. In this respect, a combination of load varying (on cartridge or cell basis) and (negative) voltage pulsing on the appropriate cells might yield interesting results.

EIS can be used during the time poisoning is taking place. This might give insight in the process of CO poisoning, by looking at the change of the model parameters over time. It might be interesting to do this on a cell basis rather than a cartridge basis, as the individual cells clearly show different responses. This should be possible already with the current setup.

*** *More about this in Addendum 1*

5 Acknowledgement

I would like to thank the EPE group for giving me the opportunity to work on this project and my coaches for their guidance. Special thanks to Marijn Uyt De Willigen and Michel van Eerd for the interesting conversations and technical support during the project. Furthermore, I would like to thank my friends and family for their moral support.

6 Literature

[01] Wingelaar, P.J.H.; Duarte, J.L.; Hendrix, M.A.M., Dynamic and static simulation tool for PEM fuel cells, IEEE ISIE 2006, Montréal, Québec, Canada..

[02] Baschuk, J.J., Row, A.M., Li Xianguo, *Modeling and Simulation of PEM Fuel Cells With CO poisoning*, Transactions of the ASME Vol. 125, June 2003.

[03] James E. Brady, Gerard E. Humiston, *General chemistry: principles and structure.* Chichester: Wiley, 1986

[04] http://hyperphysics.phy-astr.gsu.edu/hbase/hframe.html, Department of Physics and Astronomy, Georgia State University, 2006.

[05] Wingelaar, P.J.H.; Duarte, J.L.; Hendrix, M.A.M., *PEM fuel cell model representing steady-state, small-signal and large-signal characteristics*, under review Elsevier Journal of Power Sources.

[06] Brian Cook, "Introduction to fuel cells and hydrogen technology", Engineering science and education journal, December 2002.

[07] Mariana Ciureanu, Hong Wang, *Electrochemical Impedance Study of Electrode-membrane Assemblies in PEM fuel cells,* Journal of the Electrochemical Society, Nov. 1999.

[08] Friede, W.; Raël, S.; Davat, B., *Mathematical model and characterization of the transient behaviour of a PEM fuel cell*, IEEE transactions on power electronics, vol. 19, 2004.

[09] Görgün, H.; Arcak, M; Barbir, F., *An algorithm for estimation of membrane water content in PEM fuel cells*, Journal of Power Sources, 2005

[10] Hoogers, Gregor, *Fuel Cell technology handbook*, 2003, Boca Raton: CRC Press LLC

[11] Aida Rodrigues, John C. Amphlett, Ronald F. Mann, Brant A. Peppley, Pierre R. Roberge, *Carbon monoxide Poisoning of Proton-Exchange Membrane fuel cells,* Proceedings of the thirty-second intersociety energy conversion engineering conference (IECEC 97), pp 768-73 vol. 2, 1997

[12] J.J.Baschuk and Xiangua Li, *Carbon monoxide poisoning of proton exchange membrane fuel cells*, International Journal of energy Research, 25 june 2001.

[13] Thomason, A.H.; Lalk, T.R.; Appleby, T.R.; *Effect of current pulsing and "self-oxidation" on the CO tolerance of a PEM fuel cell*, Journal of Power Sources 135 (2004) 204-211.

[14] W.A. Adams, J. Blair, K.R. Bullock, C.L. Gardner, *Enhancement of the performance and reliability of CO poisoned PEM fuel cells*, Journal of Power Sources 145 (2005) 55-61.

[15] Adams, William; Gardner, Christopher L.; Dunn, James H.; US Patent 6.541.941.

[16] Choi, Woojin; Enjeti, Prasad N, Appleby, A.J.; An Advanced Power Converter Topology to Significantly Improve the CO Tolerance of the PEM Fuel Cell Power Systems, 2004 IEEE Industry Applications Conference.

[17] Carette, L.P.L; Friedrich, K.A.; Huber, M.; Stimming, U.; Improvement of CO tolerance of proton exchange membrane (PEM) fuel cells by a pulsing technique. PCCP (2000).

[18] http://www.cheminst.ca/ncw/experiments/eelectrowater.html, Chemical Institute of Canada, 2006

[19] Rozenboom; Hendrix, M.A.M., Duarte, J.L, Michon, M.M.J.A., *Low Power Electronics, Power Electronics below 2kW*, Technische Universiteit Eindhoven, 2003.

[20] Mohan, N. And Undeland T.M. and Robbins, W.P., Power electronics, Converters, Applications and Design, Third edition. Hoboken, John Wiley & Sons, Inc.

[21] Horck, F.B.M. van, *A treatise on Magnetics & Power Electronics,* Technische Universiteit Eindhoven, January 2004.

[22] Application note 848 http://www.maxim-ic.com, Maxim Integrated Products, 2005

[23] http://www.h-tec.com, h-tec Industrial, Hydrogen Energy Systems, 2006

[24] Soft Ferrites and Accessoires 2002 Data Handbook, Ferroxcube.

[25] J.J. Baschuk; Xianguo Li; *Modelling CO poisoning and O_2 bleeding in a PEM fuel cell anode*, Int. J. Energy Res. 2003;27:1095-1116.

Appendix A : Derivation of transformer equations

This derivation is partially based on the theory found in [21].

The goal of the theory presented here is to find relationships with which the transformer can be dimensioned based on restrictions such as the maximum peak current I_{max}, the maximum B-field B_{max} and the desired magnetising inductance L_m.

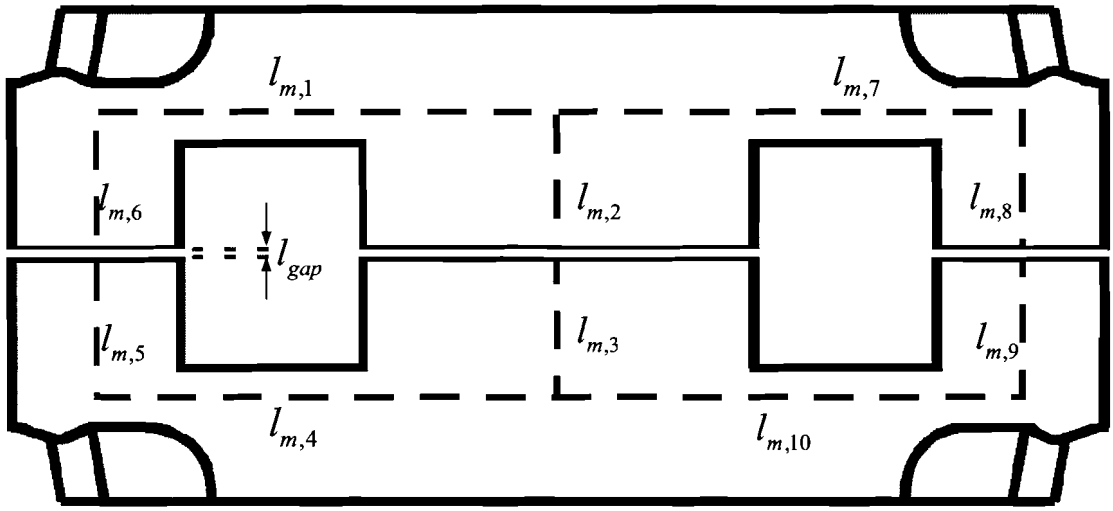

Figure 6-1: RM-12 core with indicated magnetic path lengths

From the law of Ampère-Maxwell (A.1), (A.2) can be derived

$$\oint_C \bar{H} \cdot \bar{\tau}\, dl = I_{enclosed}, \tag{A.1}$$

$$H_{core} l_m + H_{gap} l_{gap} = Ni. \tag{A.2}$$

With H_{core} and H_{gap} the magnetic fields in respectively the core and the air gap of the transformer, l_m and l_{gap} the lengths of the magnetic paths in the core and the air gap, N the number of turns and i the current through the windings. Figure 6-1 shows the magnetic paths of the chosen core, with $l_m = \sum_{n=1}^{10} l_{m,n}$. With $\phi = BA$ and $B = \mu H$, the flux becomes:

$$\phi = \mu HA. \tag{A.3}$$

Combining (A.2) with (A.3) gives

$$\frac{\phi_{core} l_m}{\mu_0 \mu_r A} + \frac{\phi_{gap} l_{gap}}{\mu_0 A} = Ni. \tag{A.4}$$

(A.4) can be re-written in a form which incorporates reluctances

$$\phi_{core}\Re_{core}+\phi_{gap}\Re_{gap}=Ni,$$
$$\Re_{core}=\frac{l_m}{\mu_0\mu_r A},\tag{A.5}$$
$$\Re_{gap}=\frac{l_{gap}}{\mu_0 A}.$$

The B-field is continuous and homogenous at the transition between air and the magnetic material and thus the flux in the core is equal to the flux in the air gap

$$\phi_{core}=\phi_{gap}=\phi,$$
$$\phi=\frac{Ni}{\Re_{core}+\Re_{gap}}.\tag{A.6}$$

An expression for the B-field can be found by combining (A.3) and (A.6) into

$$B=\frac{Ni}{\left(\Re_{core}+\Re_{gap}\right)A_e}.\tag{A.7}$$

An expression (A.8) for the maximum allowable number of turns can now be derived from (A.7):

$$N_{\max}=\frac{B_{\max}\left(\Re_{core}+\Re_{gap}\right)A_e}{i_{\max}}.\tag{A.8}$$

Vice versa, the needed air gap can also be found

$$\Re_{gap}=\frac{N_{\max}i_{\max}}{B_{\max}A_e}+\Re_{core}=\frac{l_{gap}}{\mu i_{\max}},$$
$$l_{gap}=\left(\frac{Ni_{\max}}{B_{\max}A_e}+\Re_{core}\right)\mu_0 i_{\max}=\frac{\mu_0 N i_{\max}^2}{B_{\max}A_e}+\Re_{core}\mu_0 i_{\max}.\tag{A.9}$$

The inductance is defined as

$$L=\frac{n^2}{R_{core}+R_{gap}}.\tag{A.10}$$

An expression for the magnetising inductance can be derived by squaring (A.8) and combining this with (A.6) and (A.10), resulting in

$$L_m=\frac{B_{\max}^2A_e^2\left(\Re_{core}+\Re_{gap}\right)}{i_{\max}^2}=\frac{B_{\max}^2A_e^2\left(\frac{l_m}{\mu_e A_m}+\frac{l_{gap}}{\mu_0 A_{gap}}\right)}{i_{\max}^2}.\tag{A.11}$$

Equation (A.11) can be simplified (A.12) when the air gap is present in all branches of the core. In this case, cross area of the magnetic circuit is equal to the cross area of the air gap (A_m=A_e):

$$L_m = \frac{B_{\max}^2 A_e \left(\frac{l_m}{\mu_e} + \frac{l_{gap}}{\mu_0} \right)}{i_{\max}^2}. \tag{A.12}$$

This results in a new equation for determining the required air gap

$$l_{gap} = \frac{\mu_0 i_{\max}^2 L_m}{B_{\max}^2 A_e} - \frac{\mu_0}{\mu_e} l_m \approx \frac{\mu_0 L_m i_{\max}^2}{B_{\max}^2 A_e}. \tag{A.13}$$

Finally, by combining (A.8) and (A.13) results in an expression for the maximum number of windings

$$N_{\max} = \frac{B_{\max} l_m}{i_{\max} \mu_e}(1 - A_e \mu_0) + \frac{i_{\max} L_m}{B_{\max} A_e} \approx \frac{i_{\max} L_m}{B_{\max} A_e}. \tag{A.14}$$

Appendix B : PSIM schematic for converter simulation

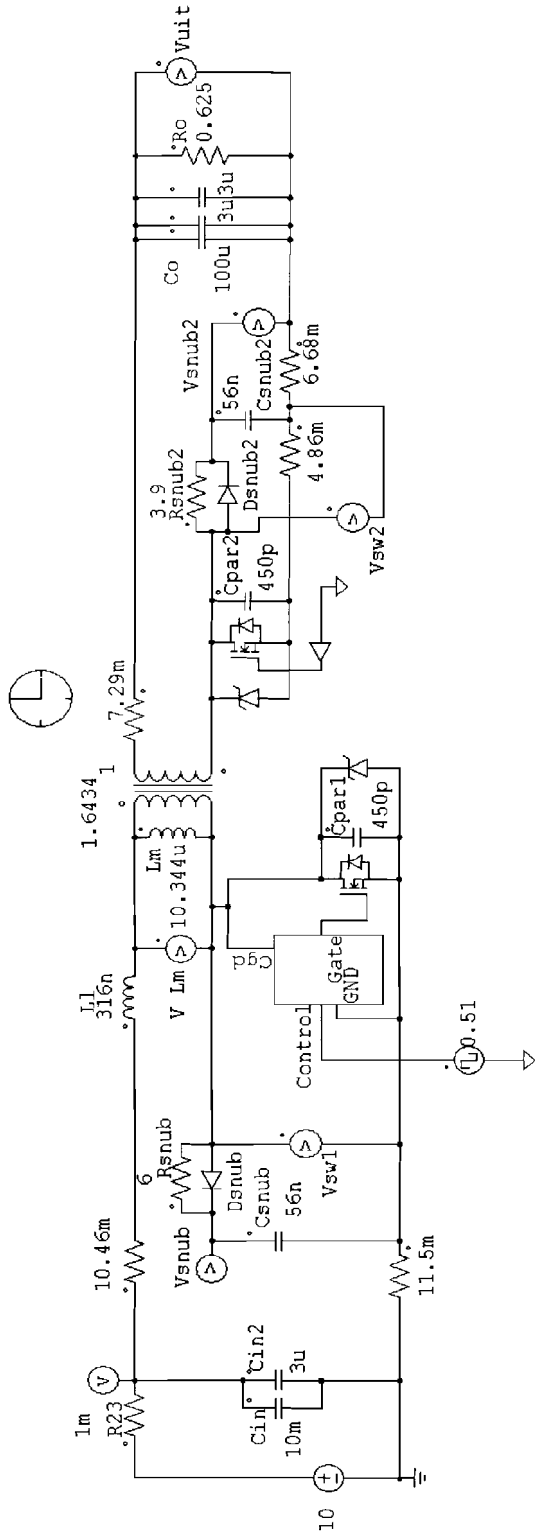

Figure 6-2: PSIM schematic used for full circuit simulation

Appendix C : Additional circuitry

C.1 Gate drivers

The gate driver on the primary side of the converter is shown in Figure 6-3. The opamp is used to buffer the dSpace gate control signal. This signal is then amplified by the 2N3904 NPN transistor and the 1kΩ resistor to ensure proper performance of the NPN-PNP totem pole formed by the BD681 and BD682 transistors. This gate driver is fed by a power source with equal ground as the primary side power circuit.

The gate driver for the secondary side of the converter is shown in Figure 6-4 and operates in a similar fashion, but it needs to be isolated from the control signal. This is done via the opto-coupler HP4503. This is an opto-coupler with a photo-sensitive diode, which controls the base voltage and current of a transistor. This gate driver is fed by an isolated power source that has a floating reference with respect to the primary side of the converter.

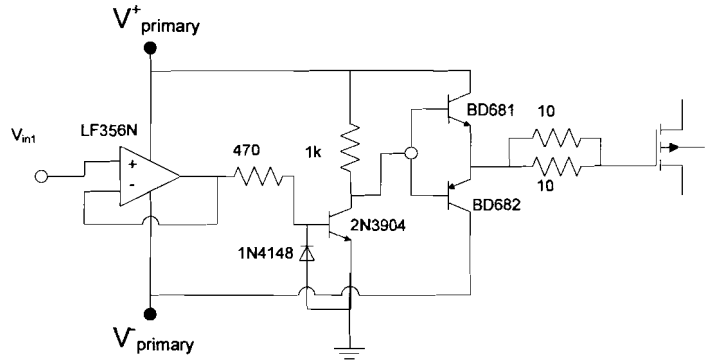

Figure 6-3: Gate driver for the primary converter side

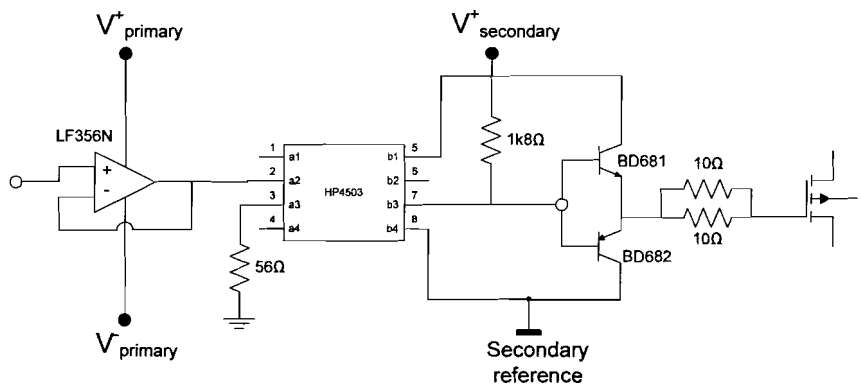

Figure 6-4: Gate driver for the secondary converter side

C.2 : Measurement circuitry

C.2.1 : Current measurement

The input and output currents are measured with the circuit given in Figure 6-5. A LEM LA25-NP current sensor is used to measure the current in the power circuit. The input-to-output current ratio is 1:1000. The 100Ω resistor is used to convert the LEM output current into a voltage. This is amplified with a factor two and 10V is substracted. This increases the utilised dynamic range of the dSpace system.

As dSpace uses its own reference, the measurement circuits are fed with a voltage centered around this reference. This measurement voltage is made with a NMA1215S DC-DC converter, with the zero output coupled to dSpace.

C.2.2 : Voltage measurement

The input and output voltages are measured with the circuit given in Figure 6-6. The V^+ and V^- supply equal the primary and secondary side supplies for respectively the input and output measurements. The measured voltage is divided by a potentiometer. The circuit makes an isolated linearly dependent version of this scaled voltage. This is done by controlling the current through the inputs of two opto-couplers, which are placed in series. The output of one of the opto-couplers is used as reference at the negative input of the opamp. The output of the other opto-coupler is the isolated representation of the input voltage. The difference between the input and output voltage of the circuit depends entirely on the measure of equality of the two opto-couplers and 1k8Ω resistors. The 15nF capacitor is used to reduce the control action performed by the opamp. The variable resistor at the input can be used to optimise the dynamic range of the measurement.

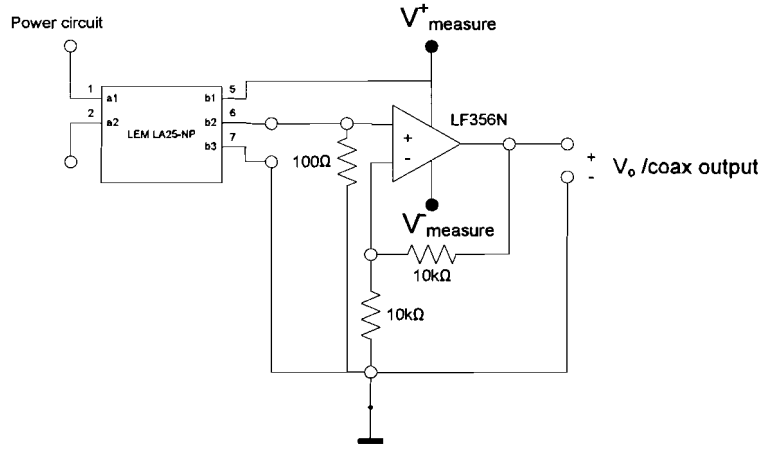

Figure 6-5: Current measurement circuit

The linearity of the voltage measurement circuitry, and the calibration are presented in Figure 6-7.

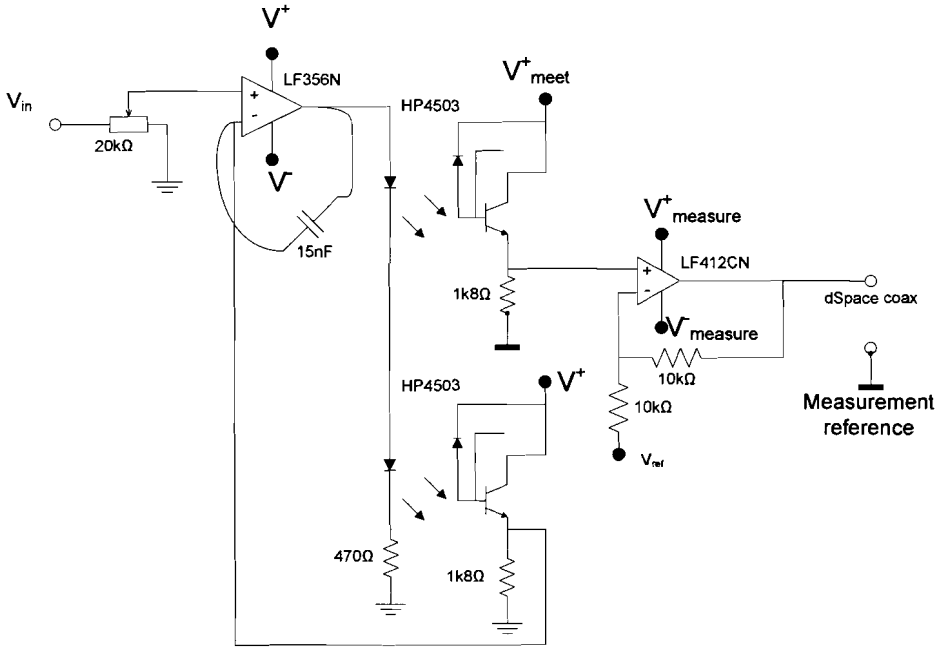

Figure 6-6: Voltage measurement circuit

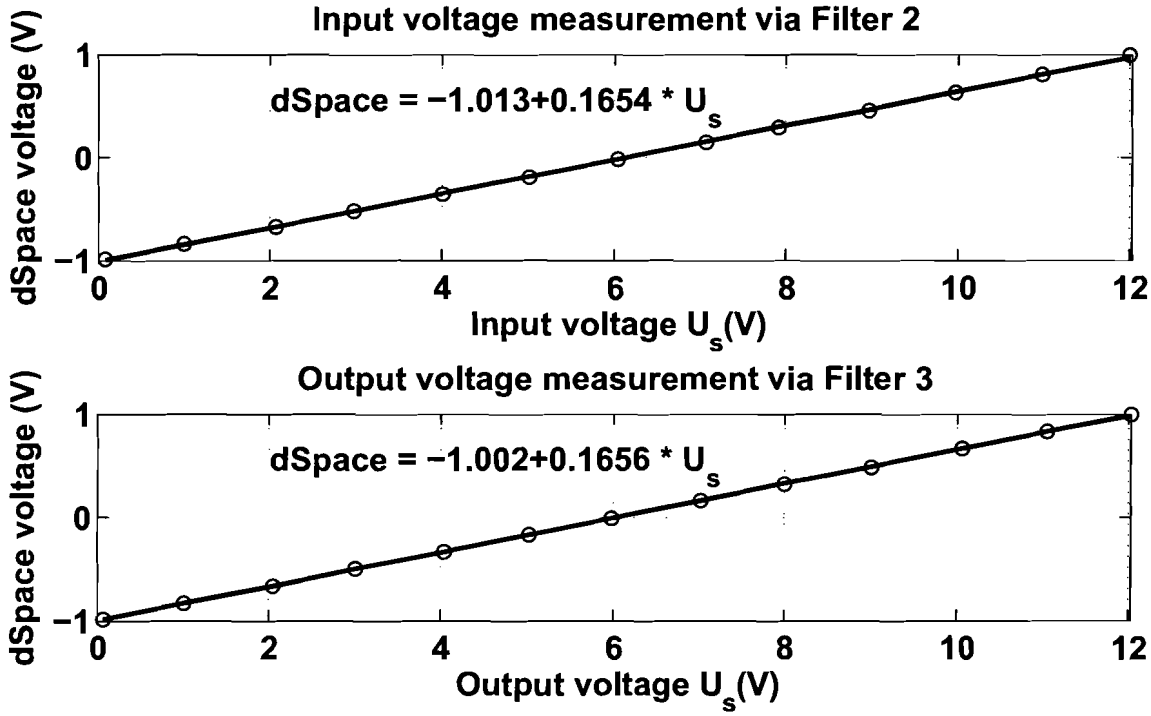

Figure 6-7: Input and output voltage measurement linearity check and calibration results

C.2.3 : Anti-aliasing filters

The dSpace system is set to a sample frequency of 10kHz. To prevent disturbances by the 100kHz ripple caused by the converter and possible noise, an anti-aliasing filter designed. The sampling is done by a 12-bit AD-converter with a range from -10V to 10V. The least significant bit equals therefore $20/2^{12}$ = 4.88mV. To prevent a false determination of the bit-value by the AD-converter, the frequencies above 5kHz should be attenuated to at least half this value: 2.44mV. The maximum voltage to be sampled is 20V. Therefore, the gain of the anti-aliasing filter has to be

$$gain_{dB} = 20 \cdot {}^{10}\log(\frac{2.44mV}{20V}) = -79dB. \quad \text{(C.1)}$$

To accomplish this, a 5th –order Butterworth filter with a cut-off frequency of 800Hz has been chosen, which has a suppression of -80.77dB at 5kHz.

Only three DA-converters are available for use with the power electronic converter, therefore three (instead of four) filters have been made. The gain graphs of these filters are shown in Figure 6-8.

The circuits deviate from their intended ideal transfer functions due to inaccuracies of the used components. The deviation is the greatest with filter 2. An overview of the attenuation at 5kHz and the -3dB corner frequencies is given in Table 2. This data indicates that filters 1 and 3 have sufficient attenuation and bandwidth. While filter 2's attenuation lacks about 11.5dB, the actual consequences of this will be limited; even if the oscillations of the converter are visible at the output of the converter, the amplitudes of these frequencies will be far less than the 20V used for calculating the filter specifications.

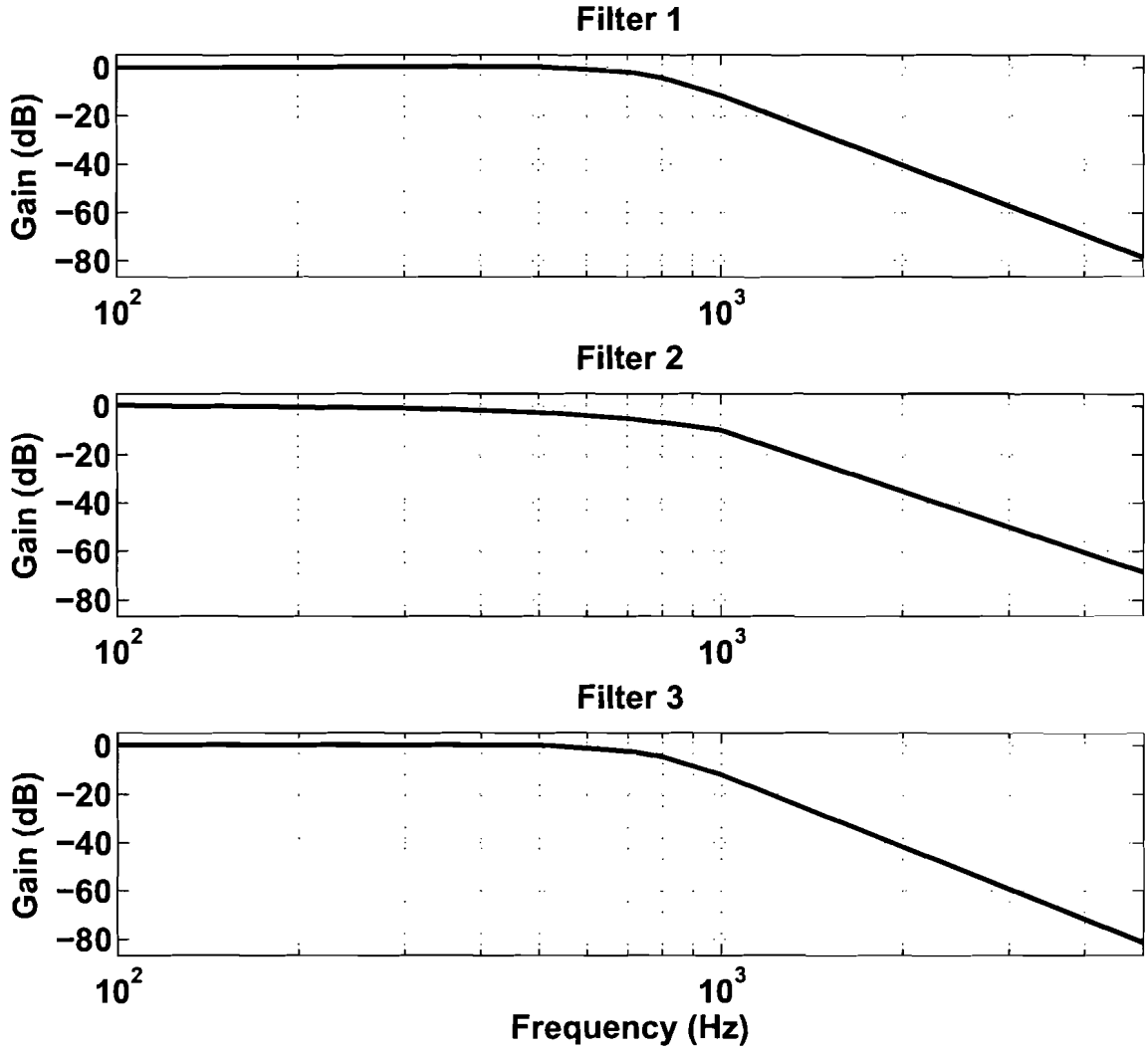

Figure 6-8: Gains of the 5th order Butterworth filters

Table 2: Attenuation at 5kHz and corner frequencies of the built filters

	Filter 1	Filter 2	Filter 3
Gain at 5kHz	$-78.7dB$	$-68.5dB$	$-81.6dB$
-3dB frequency	$\approx 755Hz$	$\approx 542Hz$	$\approx 739.1Hz$

C.3 Relay circuitry

The V23086-C2-A403 relays are used for the circuit of Figure 2-16. These are packages which contain two relays with separate coils. Two relays are put in parallel, as shown in Figure 6-9. A control signal from dSpace is buffered and a NPN transistor is turned on when the relays are switched. These relays are of the "change-over" type. The pin at which the switch is directed in off-state is not connected.

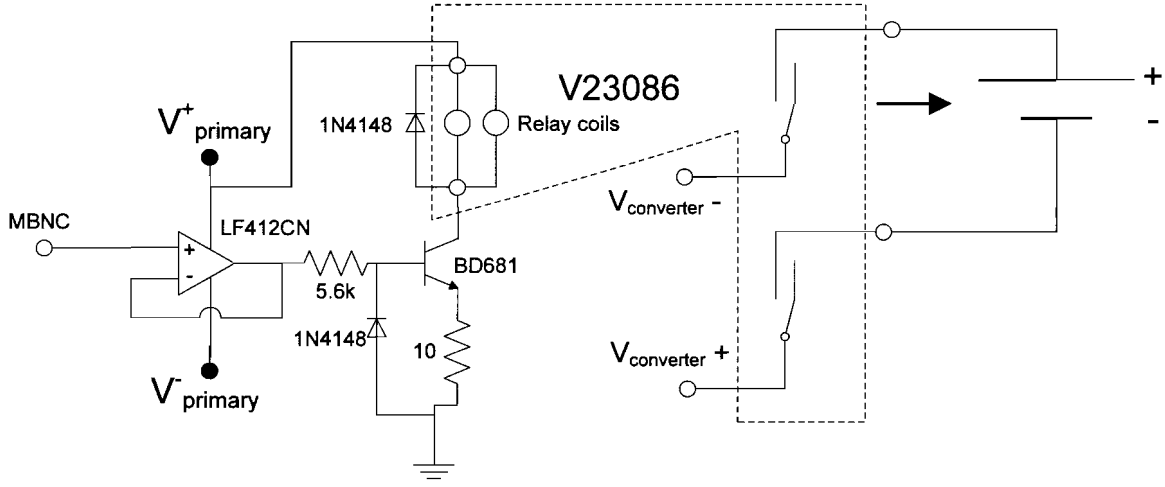

Figure 6-9: Relay control circuit

Appendix D : List of equipment

Table 3: List of equipment

Function	**Equipment type**	**Serial number / Group number**	**Manufacturer**
12V power supply (Primary converter side)		EH0361	Delta Electronics
12V power supply (Secondary converter side)	Power supply B202	EM1665	Øltronix
10V power supply (Input power supply converter)	TPS 050-5	EM 766	Delta Electronics
Input power supply / FC pulsing	XPR100-60	E00109762	Xantrex
Voltage souce load	Power supply B202	EM1473	Øltronix
Oscilloscope	AD400A	UTI-0006	Tektronix
Multimeter	PM2517X	EM 1645	Philips
Multimeter	179		Fluke
Fuel cell	SR-12		Avista Labs

Linde Gas | hoekloos

Analyse Certificaat
Certificate of analysis

HiQ Gasmengsel 4 Comp | **Artikel: R02061** *Article* | **Certificaat nr.: 35436** *Certificate nr.*

Cil. nr. *Cyl. nr.*	Waterinh. *Water cont.*	Aansluiting *Valve conn.*	Vuldruk *Cyl. pressure*	Cil. inh. *Gas volume*
1059055	5 Liter	LU4	150 Bar (15°C)	0,7 m³ (15°C, 1 Bar)

Component *Component*		Nominaal *Ordered*	Resultaat *Result*	Eenheid *Unit*	Meetonzekerheid *Uncertainty*
Koolmonoxide	CO	30	30	VPM	5 % REL
Kooldioxide	CO2	35	35,5	VOL%	2 % REL
Waterstof	H2	60	59,7	VOL%	2 % REL
Stikstof	N2			REST	

Analyse datum *Date of Analysis*
12/01/2006

Verantwoordelijk voor analyse *Responsible for analysis*
T.H.J.M. van Dick

Handtekening *Signature*

Figure 6-10: Specification of the used synthetic gas: Measurement set up

Appendix F : Boundary conditions and limitations

The following observations were made after, during or before the measurements of this section took place.

- The cartridge is not connected to the 0 of the power supply of the measurement and control circuit via a direct cable to one of the anodes or cathodes of the cells.
- The gas outlet of the cartridge is open during measurements and its state was not consequently the same in between measurements of different sections. This could have caused different degrees of poisoning for the different measurement sessions.
- The measurements presented in the following sections are well defined in terms of duration and timing. The time between series of measurements is not. This could also have an effect on the degree of poisoning of the cells.
- The detection of the cell voltage at which the load is turned off is inhibited during a pulse, to prevent a false turn-off. The "pulse on/off" signal is a bit that is switched. However, the recovery of the cell voltage is not so fast. Therefore, a broader pulse signal is used to extend the inhibition of the turn-off detection. The inhibition pulse is likely too narrow if a measurement is turned off very shortly after a pulse.
- The simulink schematic designed for the measurements of the following subsections, produced an error after it was loaded into the dSpace board and the capture was started with "stream to disk" enabled. The program could not be executed in real-time. The final solution to this problem has been to decrease the sample frequency from 10kHz to 8kHz.
- The cartridge used for these measurements is labelled 0679.

Appendix G : Measurement results

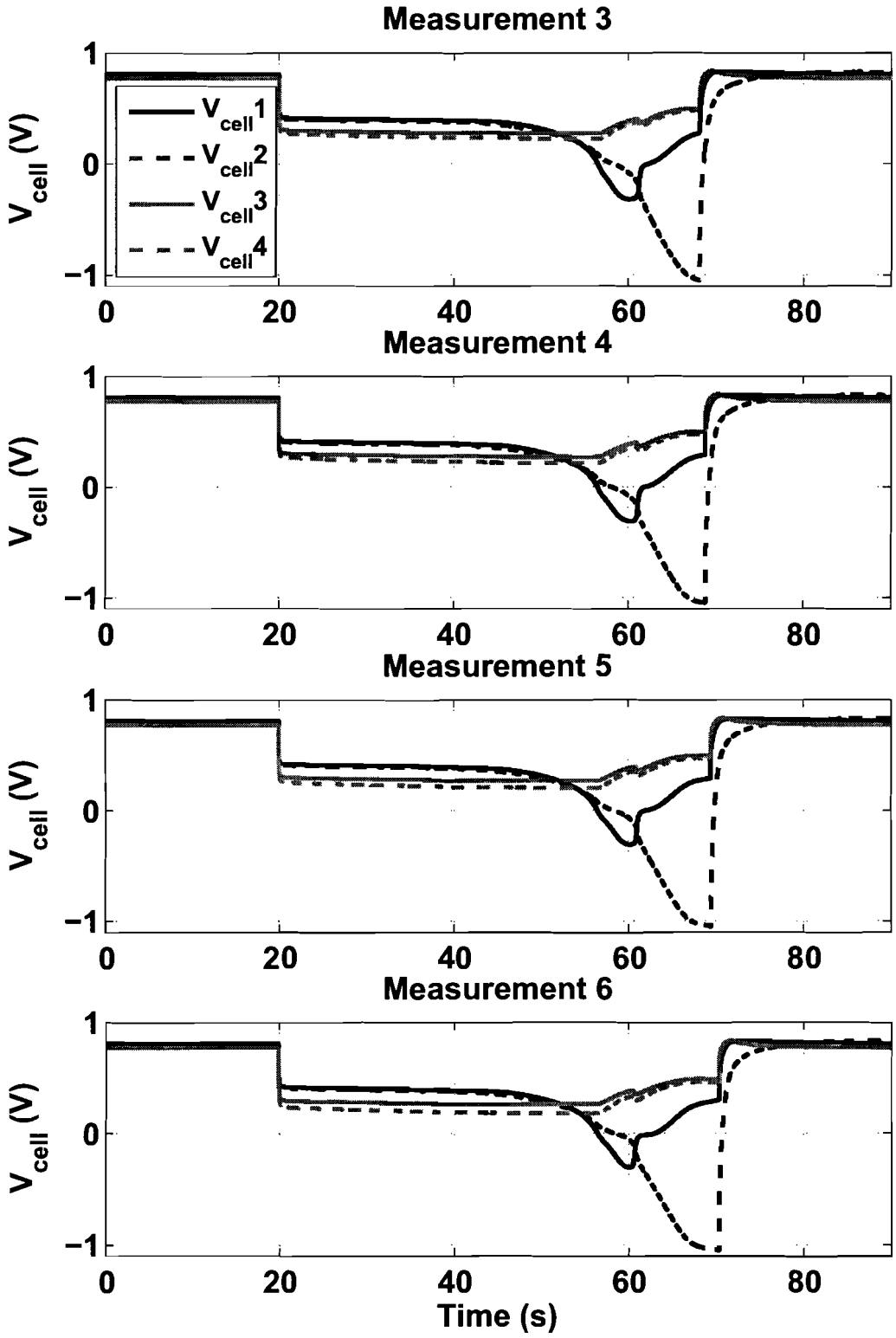

Figure 6-11: CO poisoning of the fuel cell stack at 6A load, measurements 3-6

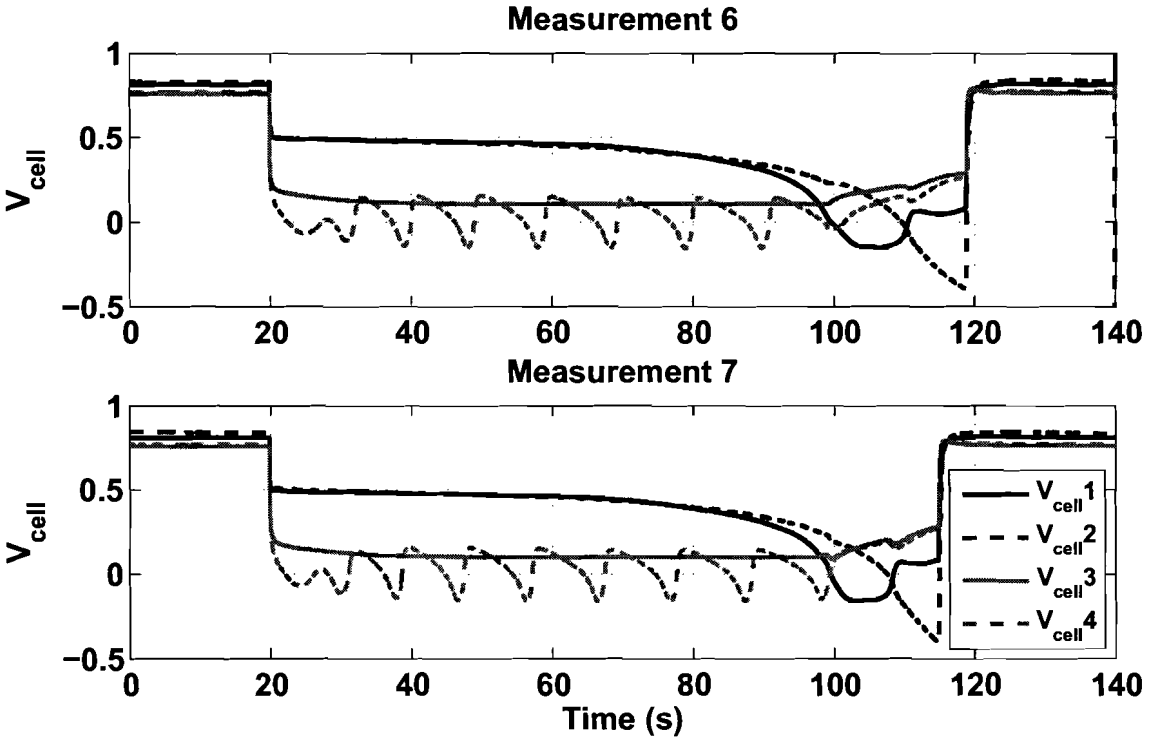

Figure 6-12: Timed pulses at 140s and planned on 160s, with a load of 4A

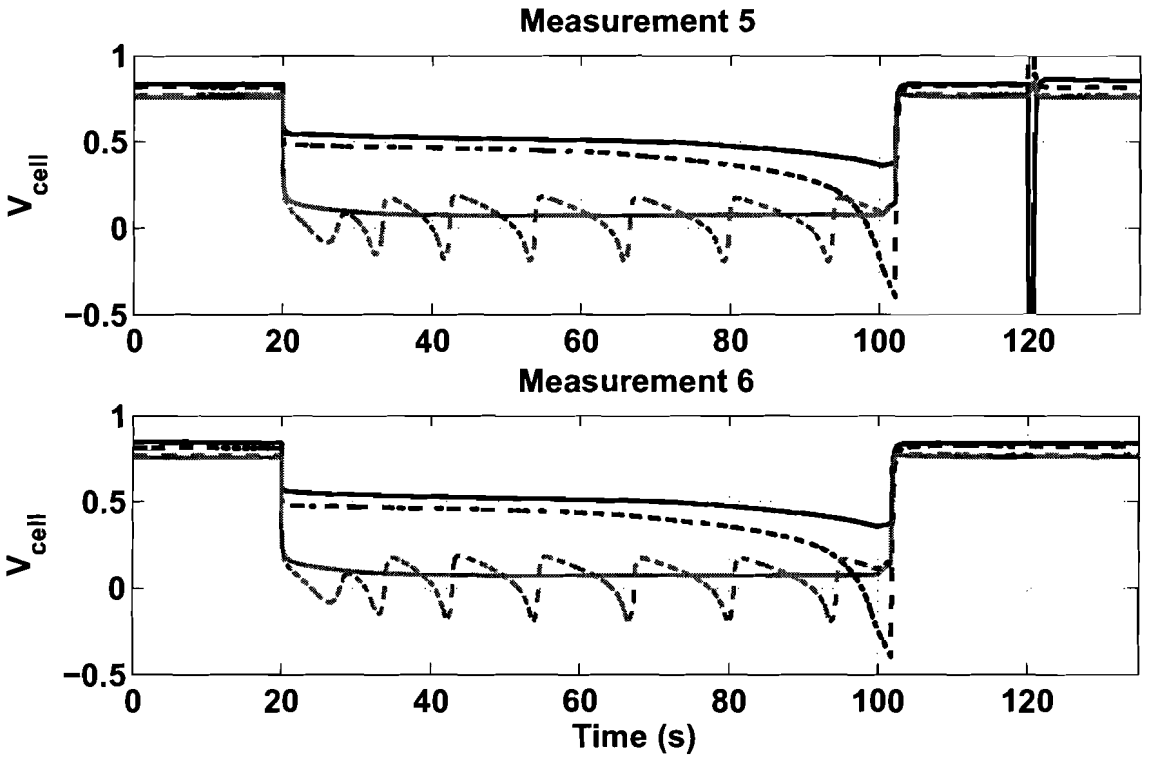

Figure 6-13: Timed pulses on cell 1 at t = 120s and 140s

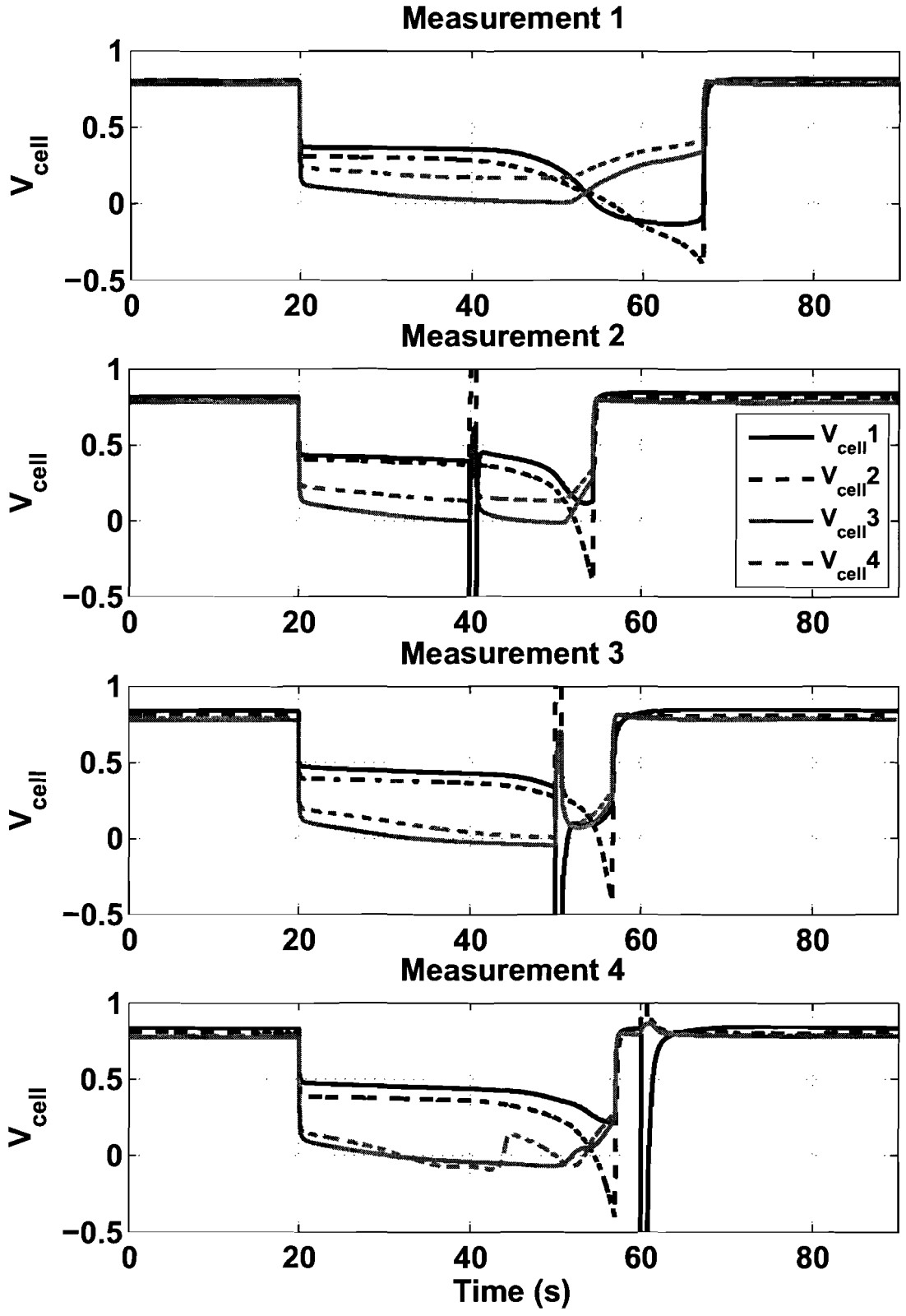

Figure 6-14: Timed pulses on cell 1 at t = 40s, 50s and 60s, with a load of 6A

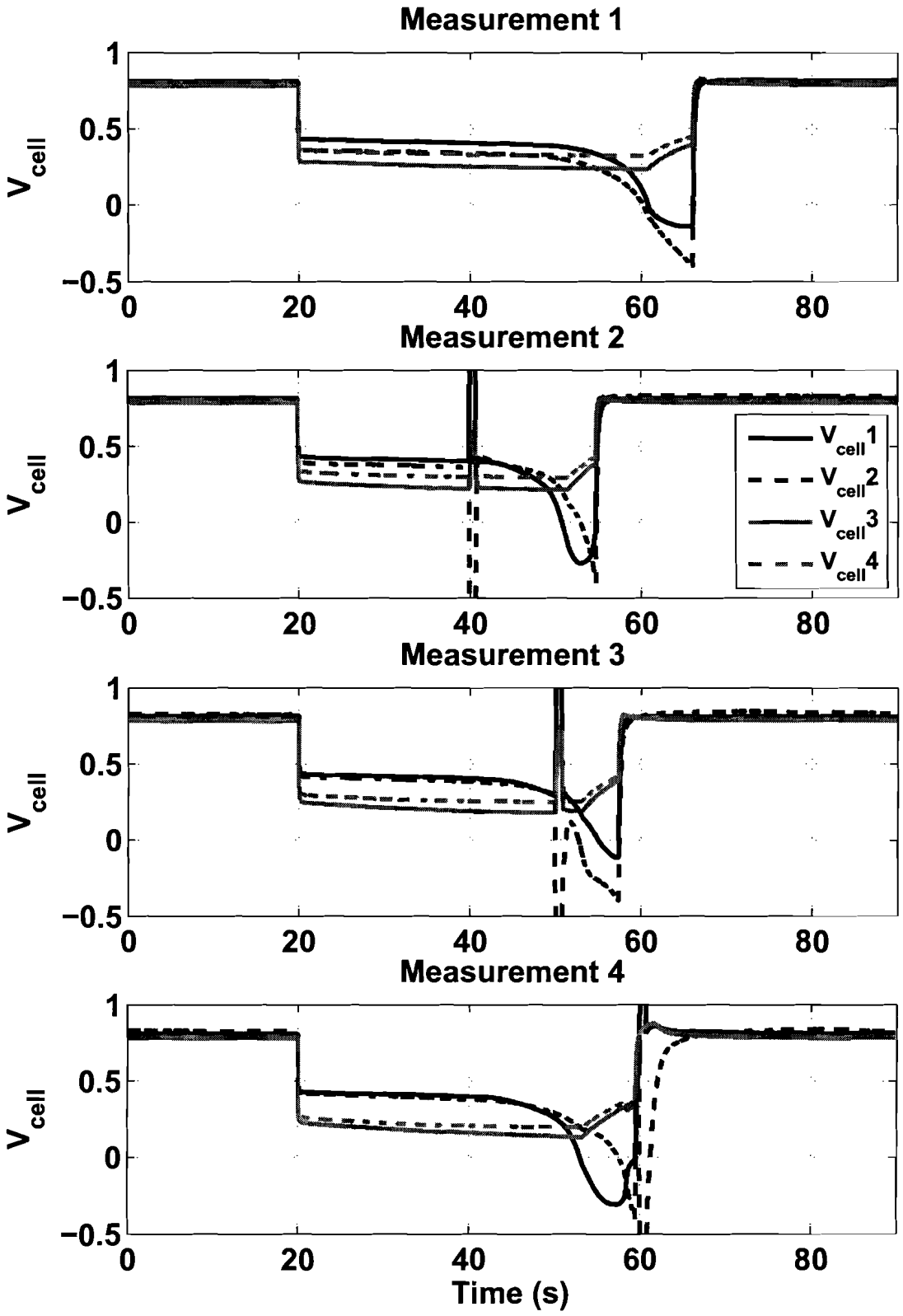

Figure 6-15: Timed pulses on cell 2 at t = 40s, 50s and 60s, with a load of 6A

Addendum 1 : Possible explanation for counter pulse

A possible explanation for the counter pulse observed has been found. The idea is inspired by the construction of the cartridge. Two metal plates are close together, giving rise to a possible parasitic capacitance in parallel to two cells. This is simulated in PSIM, using a first order model of the fuel cell construction. The simulation schematic is shown in Figure 6-18. The capacitor value needed to obtain a counter pulse in the order of what is measured (Figure 6-16), is a lot larger than what is calculated from a plate capacitor as described above. The value used in the simulation is 1F. Figure 6-17 shows the simulation result and indicates that some coupling mechanism exists between the cells similar to that used in the simulation.

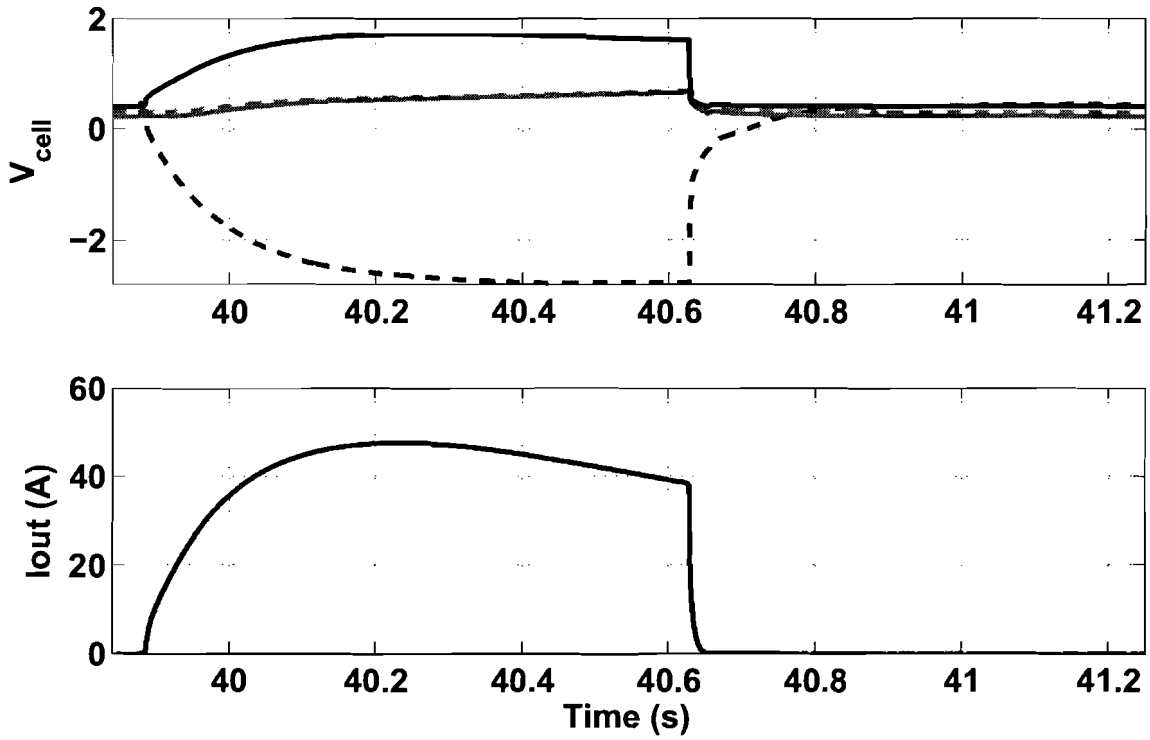

Figure 6-16: Measured pulse

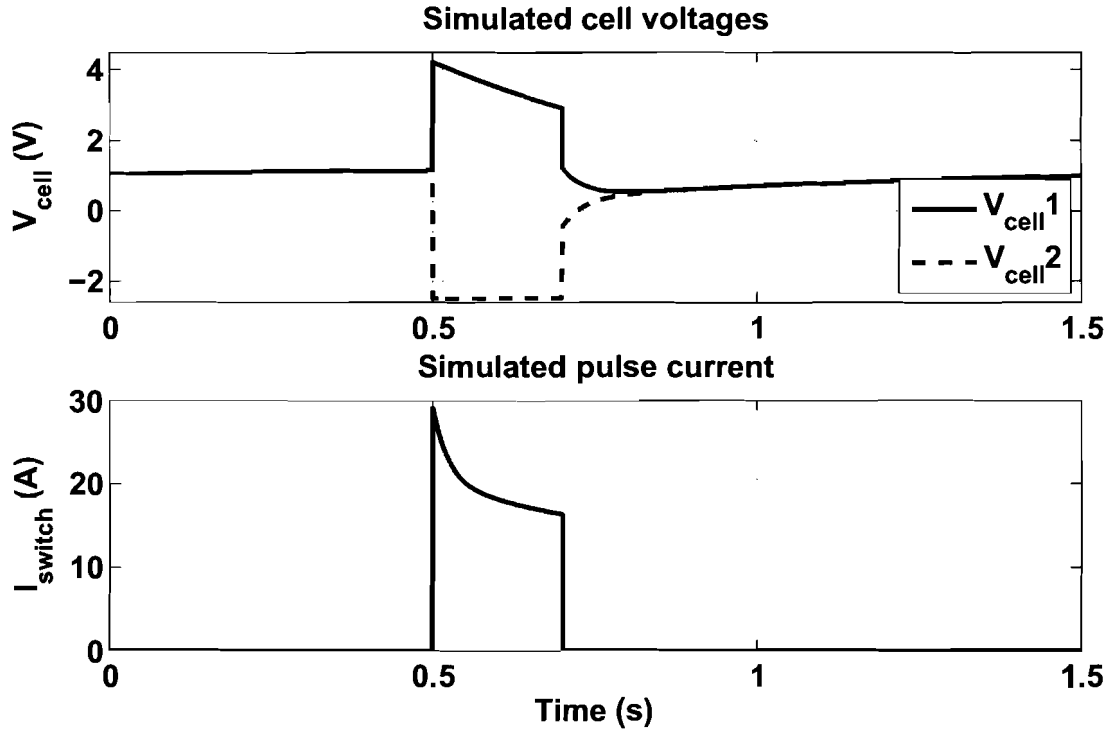

Figure 6-17: Simulated pulse

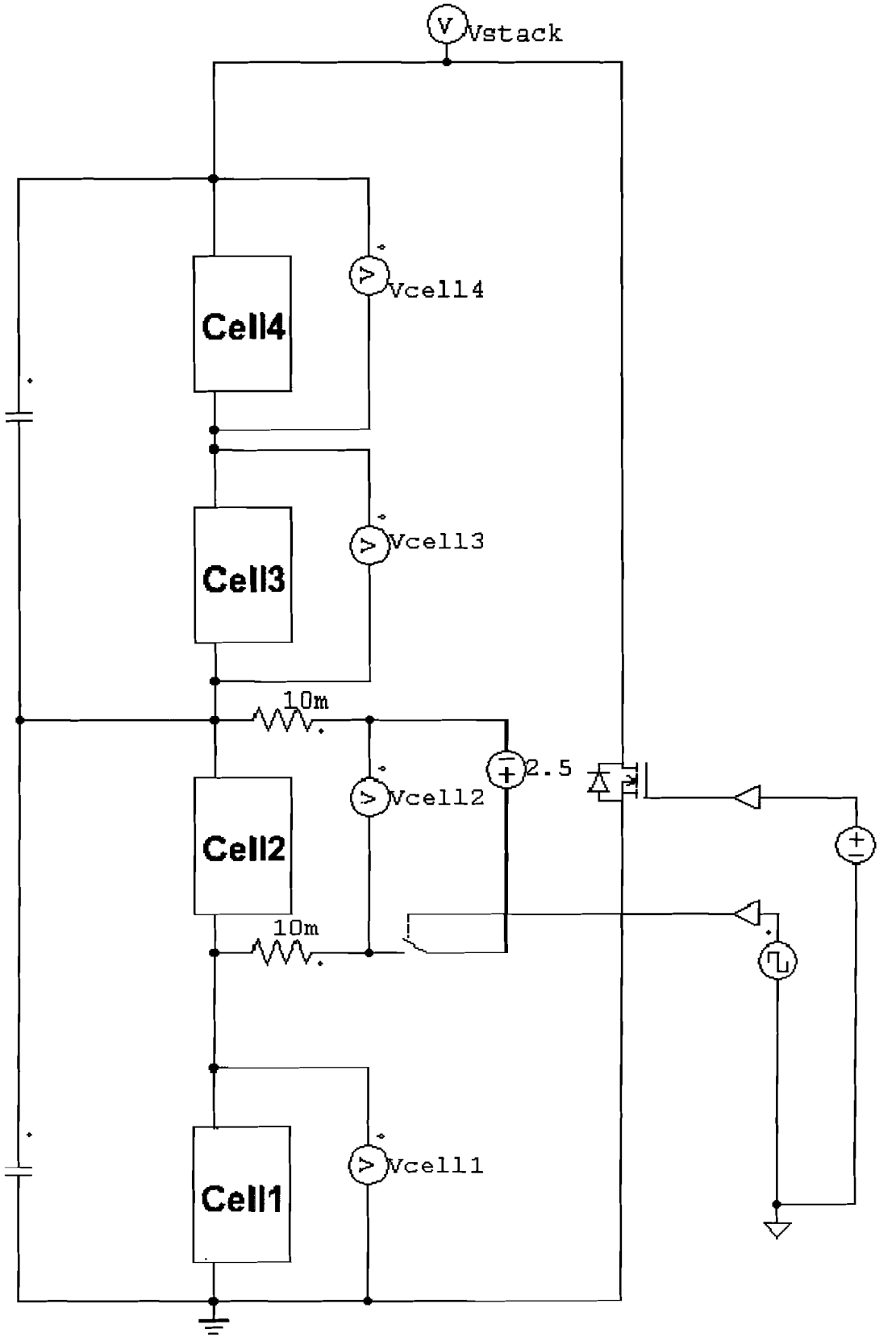

Figure 6-18: Schematic used for counter pulse simulation